Energetics and Deformation Response of Random Grain Boundaries in FCC Nickel

By

Niklas Paul Floyd

Thesis submitted to the faculty of the Virginia Polytechnic Institute and State University in partial fulfillment of the requirements for the degree of

Master of Science
In
Materials Science and Engineering

Diana Farkas, Chair
Sean G. Corcoran
William T. Reynolds

May 13, 2010
Blacksburg, VA

Keywords: Molecular dynamics, nickel, random grain boundaries, deformation, crack nucleation

Energetics and Deformation Response of Random Grain Boundaries in FCC Nickel

Niklas Paul Floyd

ABSTRACT

Molecular dynamics simulations are use to study the energetics and deformation response of random grain boundaries in polycrystalline Nickel. Computer generated samples of defect-free Ni were created, plastically deformed, and examined as a baseline understanding to the underlying mechanisms of deformation and intergranular fracture in FCC metals. Two types of samples were utilized: a sample with columnar grains consisting of pure <110> tilt boundaries and a thin-film sample with 3D grain orientations modeled after an experimental sample of austenitic steel. The structure and energies of these random boundaries under stress and temperature was analyzed. Heterogeneous displacements maps were made for a side-by-side comparison of the dislocation activity and interactions with the grain boundaries. The dislocation behavior was found to be consistent between the two digital sample types and further comparison with experimental samples was made. The intergranular cracking behavior was also studied and various factors were examined to generate general trends. Crack initiation was observed to typically occur in random high-angle boundaries close to a triple junction where the cracks have high angles with respect to the tensile loading direction. The cracking results from the simulations agree well with current preliminary results of experimentally deformed austenitic steel samples. Furthermore, the behavior and failure of the thin-film sample is compared with its corresponding experimental sample.

Acknowledgements

I would like to thank Dr. Diana Farkas who has been an excellent advisor for me. She has provided me with support and guidance that helped me throughout the duration of my graduate studies. I also thank her for the opportunity to study in such an interesting and important field, and give back my work as a contribution. The experience that I have gained is priceless, and I will always remember her.

I would like to thank my family and friends for their relentless love and support. They provided the encouragement that helped me through my research. They also kept me focused along the entire path of my undergraduate and graduate research. I would have never of made it where I am today without them.

This work was supported by the Department of Energy, Office of Basic Energy Sciences, under grant DE-FG02-08ER46525.

Attribution

One of my coworkers aided in the research and writing behind several chapters of this thesis. A brief description of her background and contribution is included below.

Dr. Diana Farkas – Professor in the Department of Materials Science and Engineering
She is my advisor and committee chair. Professor Farkas provided significant contributions and revision for chapter 2, which is currently awaiting review for publication. She also aided in the proof reading and organizing of chapters 3, 4, and 5.

Table of Contents

List of Figures

List of Tables

Chapter 1: Introduction

1.1 Problem Statement

Current steel alloys that are being used in nuclear reactor chambers, specifically those of austenitic steels, experience extreme environmental conditions consisting of high pressure, temperature, and radiation exposure, which lead to metal embrittlement and eventually fracture. In the United States, there are 104 nuclear reactor plants where the oldest reactor is 40 years old and the newest is 13 years old [1]. These reactors were originally designed and licensed for 40 years, which for many is approaching rapidly. The Nuclear Regulatory Commission (NRC) is now giving additional 20 year licenses to these old nuclear plants with the expectation that the materials will last another 50% longer [2]. The fact is, however, that many of these plants could experience failure in their steel reactor chamber components if gone undetected during inspections. Even if detected, much care and work must be done in order to replace these now heavily radioactive materials. With the push towards clean energy, nuclear power generation will continue to be utilized as an alternative source of energy, which means the 1st generation reactors will proceed to get older and new power plants will begin to be built. Current data, acknowledged by researchers and the government, show that the steel alloys in use today are experiencing failure sooner than their expected life-span [3].

In ductile materials such as the steel alloys used in nuclear reactors, the deformation process occurs by the generation and movement of dislocations, which results in the "slip" of different regions inside of the grain. The grain boundaries in metals act as both a sink and source of dislocations. As the deformation proceeds, dislocations move into and out of the grain boundaries and change the local structure. When coupled with a dislocation channel or even

dislocation pile-up, localized deformation and large changes in the boundary structure can occur. This change in the local structure affects how the material responds to the subsequent load and the increased stress and strain generated by that load. Defects such as E-units (a specific structural unit with a small hole) preexist in the grain boundary simply due to the misorientation between grains and the resulting lattice mismatch. As the strain level increases in the metal, more dislocations are generated either from the bulk grain or boundary, and cause localized deformation in the sample. Some grain boundaries do not emit dislocations due to the orientation of their preferred slip systems, which results in higher stresses around that boundary. In addition to the inherent material response, the irradiation of the metal also changes the microstructure and creates defects such as vacancies and precipitate clustering[4, 5]. This radiation exposure leads to an increase in yield strength, while decreasing the ductility of the metal, which is also known as embrittlement. Eventually over time and enough applied load, a nano-void is nucleated in the grain boundary that then grows into a crack. After the crack is formed, the specimen will eventually fracture as the crack continues to grow under load. The end result is referred to as intergranular fracture and is the leading cause of metal failure inside of nuclear reactors.

An understanding of the deformation behavior coupled with the source of intergranular crack initiation of irradiated alloys under extreme environmental conditions is necessary in order to make better life predictions and process materials with improved performance that will have a safer and longer productivity. Current experimental techniques have limited resolution at the atomic-scale, which creates difficultly when trying to examine atomic defects and interactions. Instead, computer simulations present an ideal way to model experimental samples. Their

deformation and cracking behavior can be simulated under controlled conditions while providing the atomic-level resolution needed for examining material response under load.

1.2 Overview of Computer Simulations

Computer simulations have become an increasingly important method as well as alternative to study material behavior. Specifically, atomistic simulations enable a detailed investigation of the structure and properties of materials.

1.2.1 Molecular Dynamics

For a given system with defined atomic coordinates, molecular dynamics allows the atoms to interact over a period of time where the force and motion of the individual atoms are governed by Newton's 2nd law of motion, F=ma. This law is based on classical mechanics and reproduces experimental results of atomic movements and deformation mechanisms.

The program used to run the molecular dynamics simulations was LAMMPS [6], defined as Large-scale Atomic/Molecular Massively Parallel Simulator. This program enables us to perform simulations on computers with multiple processors in way that significantly decreases the simulation time as the number of processors is increased. A code file is needed to define the parameters for the material and simulation environment, and then give instructions on the type of simulated experiment to perform. A few sample code files for different simulations can be found in the appendix. An important factor in molecular dynamics simulations is the timestep, Δt. The timestep is the amount of time between each calculation interval in which the force applied to each atom and velocities are calculated. The timesteps are repeated ($t_{i+1} = t_i + \Delta t$) until the chosen number of iterations are chosen. In order to capture the fast motion of the atoms, a femtosecond (10^{15}) timestep is required. This is one of the intrinsic limitations of molecular

dynamics, which leads to strain rates on the order of 10^7 - 10^8 s^{-1}, several orders of magnitude faster than experimental tensile tests.

Another important component in molecular dynamics simulations is the interatomic potential that describes the interactions between atoms. One reliable interatomic potential is the embedded-atom method (EAM), which mimics the interaction between atoms in metals and intermetallics [7]. The EAM model approximates the energy between two atoms as a function of distance between an atom and its neighbors. The equation which describes the potential energy of an atom is given by

$$E_i = F_\alpha \left(\sum_{i \neq j} \rho_\alpha(r_{ij}) \right) + \frac{1}{2} \sum_{i \neq j} \phi_{\alpha\beta}(r_{ij}) \qquad (Eqn\ 1.1)$$

where r_{ij} is the distance between atoms i and j, $\varphi_{\alpha\beta}$ is a pair-wise potential interaction, ρ_α is the contribution to the electron charge density from atom j at the location of atom i, and F is the embedding energy function of the atomic electron density ρ_α [8]. The present research in this thesis uses an EAM potential for Ni created by Mishin et al [9] based on empirical data and first principal calculations.

1.2.2 Computer generated samples

In addition to the interatomic potential, an initial sample configuration is necessary to perform the simulation. There are three distinct grain configurations that are typically used in atomistic simulations to study material behavior: bicrystal models, columnar polycrystalline models, and 3D polycrystalline models. Each model system has its advantage and disadvantages. Figure 1 shows a schematic drawing of each grain and grain boundary geometry.

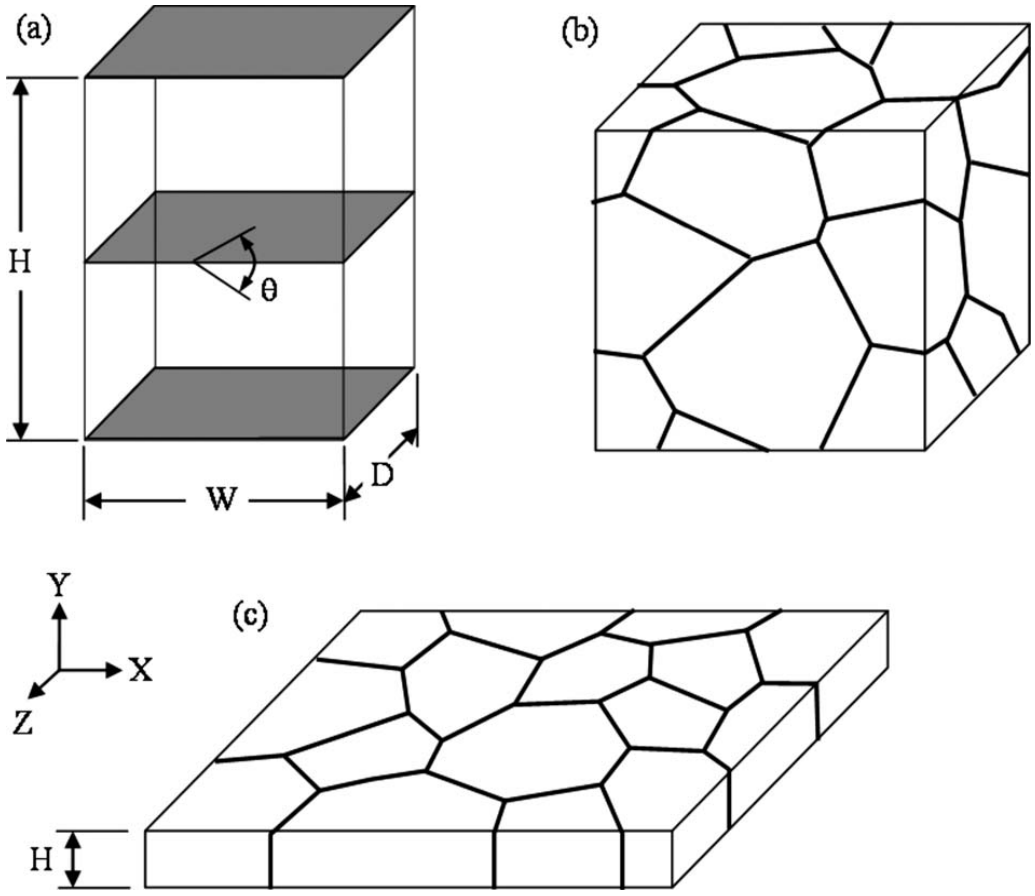

Figure 1.1 Schematic illustration of typical grain configurations used in atomistic simulations for (a) a bicrystal model, (b) a 3D polycrystalline model, and (c) a columnar grain polycrystalline model [10]. Periodic boundary conditions are usually applied.

The work presented in this research utilizes samples consisting of both the columnar grain model and the 3D polycrystalline model due to the interrelationships between mechanisms during deformation as in an actual polycrystalline microstructure. Columnar grain models have the advantage of being able to study the dislocation activity while naturally including larger grain sizes, which could move the material from the nanocrystalline region to the microcrystalline region. The disadvantage is that dislocations are restricted to certain slip systems with dislocation cores parallel to the columnar axis due to the periodic boundary conditions in the columnar direction. 3D polycrystalline models have the advantage of behaving the most similar

compared to a real polycrystalline sample. The disadvantage of this model, however, is the increased system size required to populate the entire 3D configuration. An alternative is to make a thin-film with the 3D grain continuation, except with a much smaller thickness (<10x). This method requires the use of free surfaces in the z-direction, which is typically unwanted due to additional surface effects that could be introduced during deformation.

For actual sample creation, Voronoi [11] construction is used based on the material's lattice parameter, Euler angles for grain orientation, location of grain center, and sample thickness. Figure 2 shows the sample with a reference coordinate frame defined by the axes Xs, Ys, and Zs. The Euler's angles are calculated as the angle of rotations necessary to bring the sample into coincidence with the crystal coordinate frame. As seen in the figure, there are three angles (Ψ_1, Φ, Ψ_2). In the columnar grain configuration, only two Euler angles are specific for sample creation, resulting in a sample with only tilt grain boundaries. In the 3D grain configuration, all three Euler's angles are necessary for sample creation, which results in inclined grains with both tilt and twist boundaries.

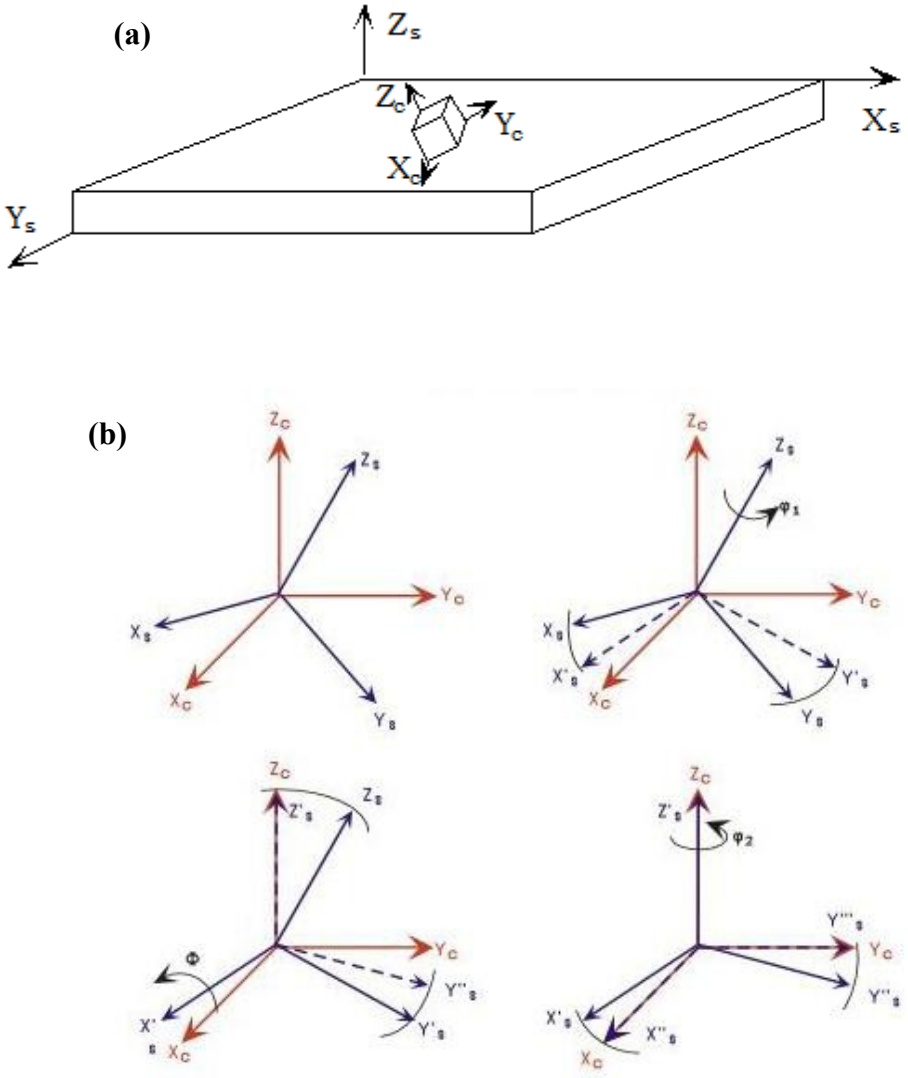

Figure 1.2 Depiction of sample coordinate frame in (a) where the necessary rotations to bring the sample into coincidence with the crystal are shown in (b). The angles of these three rotations are defined as the Euler angles.

1.3 Approach

Due to the complexity with accurately modeling an irradiated alloy, a baseline understanding to the underlying mechanisms of deformation and intergranular fracture needs to

be examined first. This thesis serves as that baseline study as well as the first step towards the initial understanding. The system is simplified by focusing on one metal, Nickel, because it has a FCC structure similar to the austenitic steels used in nuclear reactors. There are also highly accurate interatomic potentials that have been developed and extensively used for simulating nickel. The system is further simplified by focusing on a defect-free, non-irradiated sample.

The second chapter focuses on the deformation behavior of a columnar grain sample with pure tilt grain boundaries. This configuration allows detailed visualization of the structure evolution during deformation and an accurate way to calculate the grain boundary energies for correlation with the structure. The third chapter expands the sample to more complex system by introducing a 3D grain configuration. This configuration provides the most realistic deformation response and is compared with results from the columnar grain configuration. The forth chapter groups the cracking results for the samples in the 2nd and 3rd chapter in order to qualitatively and quantitatively assess the possible factors affecting intergranular crack initiation. Comparison of the cracking trends from these baseline samples is compared with results of experimental austenitic steel samples. The fifth chapter focuses on the effect of high temperature deformation and cracking as would be in the real materials. This allows for further comparison of the baseline samples with the experimental samples.

1.4 References

1. *U.S. Nuclear Power Plants*. Nuclear Energy Institute 2009; Available from: http://www.nei.org/resourcesandstats/nuclear_statistics/usnuclearpowerplants.
2. *U.S. Nuclear Power Plant License Information*. Nuclear Energy Institute 2009; Available from: http://www.nei.org/resourcesandstats/nuclear_statistics/licenserenewal.
3. *Contentions in the matter of license renewal for DUKE McGuire Nuclear Stations 1 and 2 and Catawba Nuclear Stations 1 and 2*, in *United States of America Nuclear Regulatory Commission before the Atomic Safety and Licensing Board*. 2001, Blue Ridge Environmental Defense League.

4. Onchi, T., et al., *Crack initiation mechanism in non-ductile cracking of irradiated 304L stainless steels under BWR water environment.* Journal of Nuclear Science and Technology, 2006. **43**(8): p. 851-865.
5. Miller, M.K. and K.F. Russell, *Embrittlement of RPV steels: An atom probe tomography perspective.* Journal of Nuclear Materials, 2007. **371**(1-3): p. 145-160.
6. Plimpton, S., *Fast Parallel Algorithms for Short-Range Molecular Dynamics.* Journal of Computational Physics, 1995. **117**(1): p. 1-19.
7. Daw, M.S. and M.I. Baskes, *Embedded-Atom Method - Derivation and Application to Impurities, Surfaces, and Other Defects in Metals.* Physical Review B, 1984. **29**(12): p. 6443-6453.
8. *Pair-EAM*. LAMMPS Molecular Dynamics Simulator 2010; Available from: http://lammps.sandia.gov/doc/pair_eam.html.
9. Mishin, Y., et al., *Interatomic potentials for monoatomic metals from experimental data and ab initio calculations.* Physical Review B, 1999. **59**(5): p. 3393-3407.
10. Spearot, D.E. and D.L. McDowell, *Atomistic Modeling of Grain Boundaries and Dislocation Processes in Metallic Polycrystalline Materials.* Journal of Engineering Materials and Technology-Transactions of the Asme, 2009. **131**(4).
11. Farkas, D. and W.A. Curtin, *Plastic deformation mechanisms in nanocrystalline columnar grain structures.* Materials Science and Engineering a-Structural Materials Properties Microstructure and Processing, 2005. **412**(1-2): p. 316-322.

Chapter 2: Energetics and Plastic Deformation Behavior of <110> Random Tilt Grain Boundaries

By Niklas Floyd and Diana Farkas

2.1 Abstract

Molecular dynamics simulations are used to study the grain boundary energies for random misorientation and grain boundary planes in a model FCC polycrystalline digital sample with random <110> tilt boundaries. The atomistic approach utilized a volume dependent interatomic potential for Ni and a columnar grain configuration was used to analyze the excess potential energy behavior of the grain boundaries as a function of temperature, plastic deformation and relaxation state. The results for the random tilt boundaries were compared to those of symmetric tilt boundaries with regards to energy dependence on misorientation. We further discuss the nature of the dislocation emission process in the random tilt boundaries and compare it to the case of symmetrical tilt boundaries. Finally, the effects of grain boundary relaxation state on the mechanical response are analyzed.

2.2 Introduction

Grain boundary (GB) engineering has played a vital role in improving the performance of many metallic materials over the past few decades due to the effect that GB's have on the materials' properties [1]. One example is the directional solidification and single crystal growth of gas turbine blades to help improve creep resistance during their extremely high temperature operation. The importance of grain boundary energy and structure behavior in materials has been studied in many cases using computer simulations [1-9]. However, most simulation work to date models only special cases such as perfectly symmetrical tilt boundaries [2, 3, 8]. In the

present study, we use a large polycrystalline sample (~10^7 atoms) with all random boundaries of only tilt characteristic with the goal of understanding the behavior of more general random boundaries.

We focus on random boundaries because most GB's in real polycrystalline materials are asymmetrical. There is also plenty of experimental data on energy measurements and simulations of symmetrical tilt boundaries to allow for easier comparison with the simulation trend results [10-12].

This paper studies the effects of tensile deformation and temperature on the potential grain boundary energy in a virtual FCC polycrystalline sample of Ni. We use a columnar grain structure and a [110] texture to visualize the sample in a mostly quasi-2Dimensional orientation. Columnar grain structures represent an ideal way to extend simulation work done in bicrystals with symmetrical tilt containing special boundaries to polycrystals with more general boundaries [13]. We also relax the sample at two different temperatures, 300K and 700K, to see the effects of equilibration and the relaxation state of the boundaries on the computer-generated grain boundary structure. The atomic interaction is modeled through Molecular Dynamics by using the Mishin Ni [14] interatomic potential via the embedded atom method (EAM) inside of the program LAMMPS [15].

2.3 Methodology

2.3.1 Simulation Technique

The grain and grain boundary network for the sample was generated using a standard Voronoi construction [16] with random grain orientation and boundary misorientation angles tilted around the <110> axis such that all the boundaries are of only tilt characteristic. The digital sample contains 9 grains that are approximately 40nm in diameter and uses a 2D

columnar grain structure with periodic boundary conditions in the x-, y-, and z-direction as shown in Figure 1. The periodic boundary conditions help eliminate the free surface effects. The <110> tilt axis was chosen so that each grain would have slip systems available along two different (111) type planes. There is a total of 25 grain boundaries in the sample. The sample contains random high-angle (RHA), random low-angle (RLA) and Σ3 boundaries, similar to the sample creation in Farkas and Patrick [13].

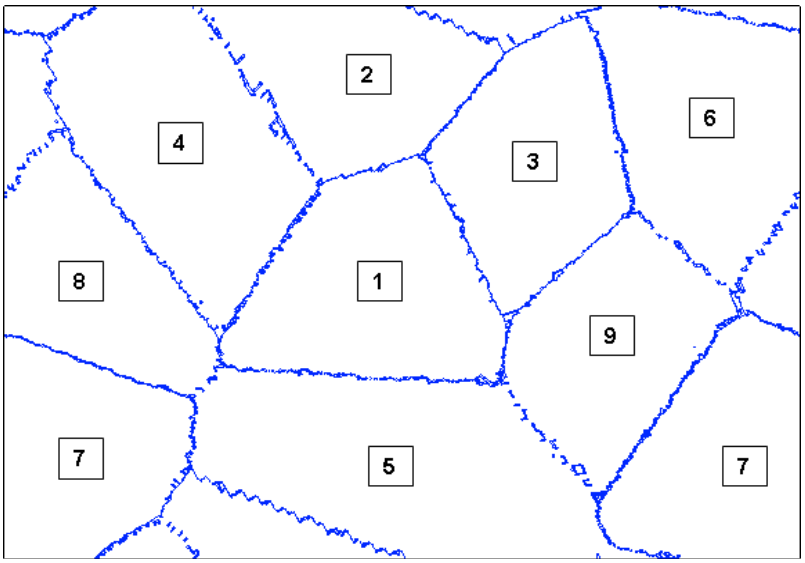

Figure 1.1 Sample configuration with 9 grains, approx. 40nm in diameter, relaxed by heating to 1200K and cooling back to 300K in 450ps.

The atomistic simulation approach used here utilizes Molecular Dynamics based on one widely used interatomic-potential, the Mishin Ni potential via the embedded-atom method (EAM) [14]. This potential appropriately reproduces the energies of stable and metastable structures, which has been a problem for many other potential models [17]. The molecular dynamics implementation was that of the program LAMMPS [15]. The boundaries in the digital sample were relaxed using two methods for deformation comparison: (1) room temperature (RT) relaxation at 300K for 30 picoseconds and (2) high temperature (HT) relaxation via a thermal treatment of 300K to 1200K to 300K for 450 picoseconds. Vo et al. [18] argues that

high temperature annealing is crucial for equilibrating GB's in computer generated polycrystals. For examining GB energy response to plasticity, the sample was deformed in the Y-direction at a rate of 3.3×10^{8} s^{-1} up to 15% strain, and data for individual atoms was recorded every 1% strain including atomic position, centrosymmetry parameter [19], potential energy, stress, and coordination number. For examining the trends of GB potential energy as a function of temperature, the sample was heated to 1200 K in 100 ps and the temperature was monotonically decreased from 1200K over a period of 400 picoseconds with data recorded at the following temperatures (K): 55, 300, 400, 750, 850, and 1200.

2.3.2 GB energy calculation

In many previous simulation studies, the grain boundary energy is obtained by using similar symmetrical tilt bi-crystal set-ups [2, 8]. The grain boundary energy is a result of the excess energy difference between a perfect sample and a sample of the same material with the grain boundary present.

Instead of the bi-crystal method, the present work shows energy calculations on a 2D sample of random boundaries to gauge the grain boundary energy response to temperature and more importantly, deformation while keeping the simulation cell as large as possible to avoid nano-size effects and more accurately describe a real material. The energy was measured by selecting a region of atoms around the boundary with a width large enough to include all of the atoms affected by the presence of the lattice misorientation between the two grains. This was determined to be approximately 15Å on either side of the boundary. The perfect lattice energy for each grain involved in the GB as a function of temperature and deformation level was obtained by measuring the average potential energy per atom in a region that included no defects. Similar to bi-crystal energy measurements, we calculate the difference in the total potential

energy of the selected region and the potential energy of the same number of atoms in a region without any defects under the same temperature and strain conditions. This excess energy is divided by the cross sectional area of grain boundary present to obtain the grain boundary energy. In our undeformed sample at 300K, this gives us rather accurate energy measurements; however, as deformation is increased or the temperature of the sample is increased, the level of accuracy decreases and the error associated with this type of selection measurement becomes larger, due to possible inhomogeneities in the strain and thermal vibrations.

The error in these measurements is estimated based on the two standard deviations found in the defect-free energy within an individual grain, and the possible differences in the average defect-free energy per atom between the two grains making up the grain boundary. The selected widths of a boundary of about 30 Å is made small enough to reduce the amount of error added from extra atoms, but large enough to fully include all boundary affected atoms. The combination of these two sources allows for reasonable error estimates of our GB energy calculations. In addition to these error estimates, our results are also subject to the standard intrinsic limitations of the interatomic potential chosen.

2.3.3 Sample Deformation procedure

The sample was deformed in a strain controlled environment up to 15% strain for each relaxation treatment. The displacement-controlled deformation of the digital samples was performed using standard molecular dynamics at room temperature, which was controlled by a Nose-Hoover thermostat and barostat to result in zero pressure in the directions perpendicular to the tensile axis. We utilized a strain rate, $3x10^{8}$ s^{-1}, that was as slow as possible with the available computing power.

2.4 Results

2.4.1 Energies of the random <110> tilt boundaries as a function of misorientation angle

The dependence of potential GB energy with misorientation was investigated for the sample relaxed at 300K. At the same 300K, the calculated potential grain boundary energy (E_{gb}) and corresponding misorientation angle (Θ_{mis}) around <110> for each boundary in the digital sample can be seen in Table 1. The lowest energy is 0.88 J/m^2 whereas the highest energy is 1.66 J/m^2. The average E_{gb} is 1.34 J/m^2 with a standard deviation of 0.21. We classified the grain boundaries into the various possible types (i.e. RHA, RLA, Σ=3, Σ=11, etc.) based on the grain boundary misorientation and using the Brandon criterion for tolerance [20]. Our sample consisted of 58% RHA boundaries while the remaining were 23% RLA and 19% CSL-type boundaries. Due to twinning, many experimental samples of pure Ni indicate a significantly higher ratio of Σ3 boundaries, often greater than 50%, while general/high-angle boundaries represent only about 25% of the entire grain boundary population [21]. Our grain boundary type distribution is a result of purely random choice of grain orientations.

GB Number	Θ_{mis} (°)	E_{gb} (J/m^2)	Type
1-2	80.19	1.09	RHA
1-3	125.42	1.08	Σ11
1-4	88.93	1.56	RHA
1-5	156.51	1.43	RHA
1-8	147.13	1.48	RHA
1-9	149.71	1.66	RHA
2-3	154.39	1.57	RHA
2-4	171.26	1.38	Low-angle
2-5	103.68	1.28	Σ3
2-7	97.90	1.35	RHA
3-5	77.80	0.88	Σ3
3-6	102.53	1.37	Σ3
3-9	85.57	1.19	RHA
4-6	111.72	1.34	Σ3
4-7	90.00	1.44	RHA
4-8	121.18	1.41	RHA
5-7a	21.34	1.59	RHA
5-7b	25.24	1.40	RHA
5-8	171.07	1.28	Low-angle
5-9	7.51	1.29	Low-angle
6-7	158.70	1.44	RHA
6-8	170.63	1.22	Low-angle
6-9	171.89	1.07	Low-angle
7-8	149.89	1.55	RHA
7-9	151.15	1.62	RHA
8-9	2.00	0.91	Low-angle

Table 1.1 Grain boundary data for each boundary in the undeformed Ni sample relaxed at 300K for 450ps, including misorientation angle about [110], potential energy at 300K, and GB type.

In order to visualize the results, the grain boundary energies are plotted as a function of the misorientation about [110] as shown in Figure 2. For comparison with symmetrical tilt boundaries, the results of simulated, perfectly symmetric <110> tilt-boundary energies calculated by Lee and Choi [17] at 0K for Al is overlaid on top of our data and normalized to the maximum grain boundary energy. For symmetrical tilt boundaries in Al, it was shown that the simulated and experimental measurements and trends agree well [17]. Figure 2 shows that the calculated energies from our simulation follow the same trends obtained in reports for <110> symmetric tilt GB's [17, 22, 23]. These trends include noticeable cusps in E_{gb} at the (111) twin boundary (Σ3 at 70^o), the (113) twin boundary (Σ11 at 129^o), and low-angle misorientations. There was also a

small cusp located at 109°, which agrees with the (112) symmetrical tilt Σ3 boundary in the simulation work of Lee and Choi [17], but is hardly seen in the experimental measurements performed at high temperatures [22, 23] or in a high temperature annealed sample [21].

Our results show that random <110> tilt boundaries present a dependence on misorientation angle that is quite similar to that observed in symmetrical tilt boundaries. The most important difference in the trends is that the cusps corresponding to CSL boundaries tend to be less deep, due to the random locations of grain boundary planes not taking full advantage of the coincident lattice.

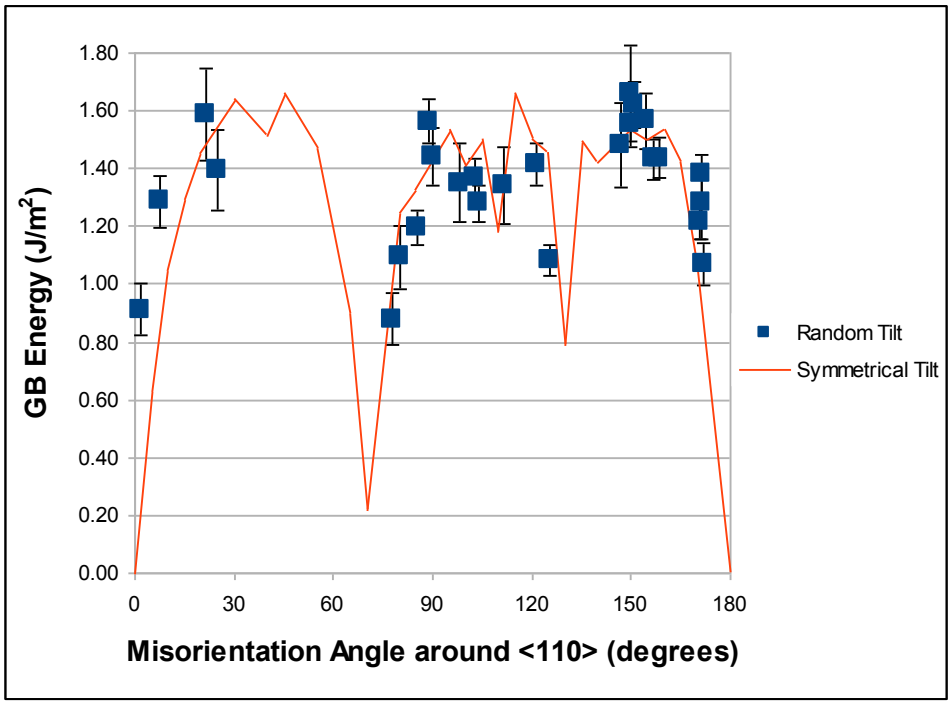

Figure 2.2 Chart of GB energy as a function of misorientation angle around [110]. Random tilt boundary energy for Ni (blue) and corresponding symmetrical tilt data from reference [3] (red) normalized using the highest GB energy.

2.4.2 Variation of the energy along the boundary and the effects of grain boundary relaxation

For symmetrical tilt boundaries, the grain boundary energy is constant over the length of the boundary. For our digital sample, relaxed at 300K, we studied five grain boundaries, GB1-5,

3-6, 4-8, 2-5, and 7-9, to see how the energy varied along the length of the same boundary. Figure 3 shows a map of the sectioned GB's with their corresponding energies. In each of the boundaries, the GB energy was different in at least one of the three sections made in that boundary by amounts larger than our estimated error. This suggests that in random boundaries, the energy can vary significantly along the length of the boundary. The largest energy difference between sections was in GB 7-9, which had a range of values differing by 0.437 J/m^2, well outside the estimated error.

The energies of the boundaries were also affected by the relaxation process that we chose for the sample. When the samples were relaxed using the high temperature treatment, the grain boundary energy was lower, with an average GB energy over all 25 boundaries of 1.12 J/m^2 instead of 1.32, which we obtained for the low temperature relaxation. This average energy difference due to the different relaxation treatments is smaller than the energy variations that we observe when considering grain boundary regions within a single boundary. Nevertheless, the high temperature relaxation treatment yields average grain boundary energies that are close to 20% lower than those found for the boundaries relaxed at 300K, a significant difference. As we will describe in the following sections, this results in differences in the response of the boundaries to deformation.

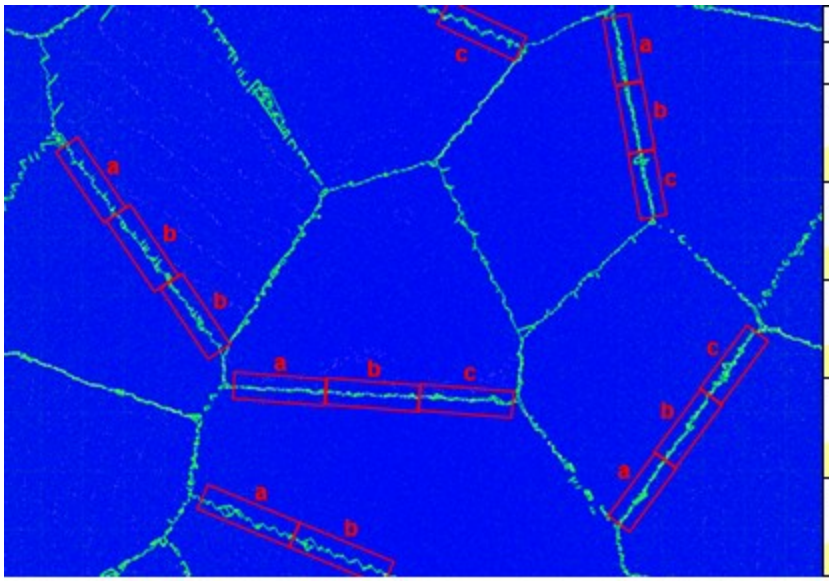

Grain Boundary Energy (J/m^2)		
(a)	(b)	(c)
GB 1-5		
1.534	1.338	1.521
Full Length =		1.432
GB 3-6		
1.39	1.212	1.491
Full Length =		1.367
GB 4-8		
1.393	1.346	1.504
Full Length =		1.414
GB 2-5		
1.408	1.332	1.131
Full Length =		1.280
GB 7-9		
1.585	1.439	1.876
Full Length =		1.620

Figure 2.3 Map of sectioned GB's in the sample relaxed at 300K. Three difference sections were taken per each boundary as indicated by a, b, c. The energies calculated for each section are indicated as well as the overall energies for each grain boundary.

2.4.3 Potential energy of the grain boundaries as a function of temperature

The sample temperature was first increased to 1200K in 100ps and then decreased from 1200K to 300K in 400ps. Grain boundary potential energy data was collected along various temperature intervals during the cooling process for specific grain boundaries present in our sample: low-angle, high-angle, and Σ3 boundaries. Two boundaries of each type were analyzed for a total of six boundaries. As seen in Figure 4, the potential grain boundary energy for each boundary increases as the temperature of the sample increases. A trend-line was fitted to each measured grain boundary using a linear regression line, which showed a good correlation of greater than 77% for all the fits with an average fit correlation of 85%. One should note that these are the total excess potential energies of the boundary as opposed to excess free energy, which is typically used when referring to GB energy at high temperature. In our sample, the total potential energy increases with temperature, but if considering the excess free energy, then

the excess entropy contributions typically result in GB free energies decreasing with increasing temperature [9, 24, 25].

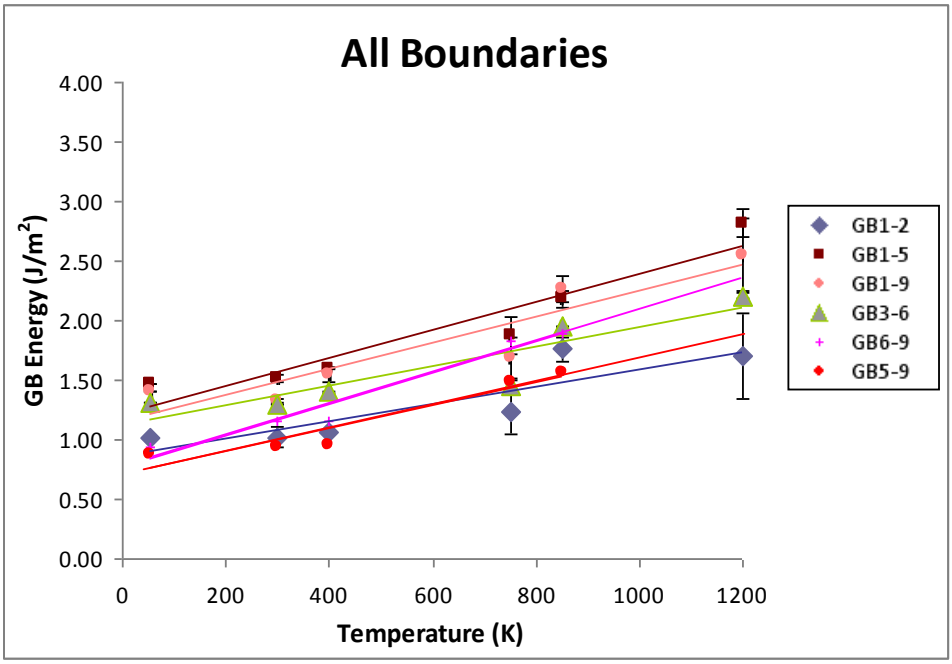

Figure 2.4 Grain boundary potential energy versus temperature for six different boundaries in the sample.

2.4.4 Grain boundary response to deformation

The digital sample was plastically deformed to 15% strain, in a strain controlled simulation. As the deformation process progressed during the simulation, the grain boundaries in the sample emitted and absorbed dislocations. We observed the emission of Shockley partial dislocations, resulting in stacking faults that were in some cases followed by the emission of trailing partial dislocations. Although some boundaries experienced more dislocation activity than others, all the GB's participated as a sink and/or source for dislocations, and no dislocations were observed to be transmitted across the set of grain boundaries in our simulations. The deformation process led to local changes in the boundary structure [13]. An example of dislocation emission at the GB can be seen in Figure 5: Shockley partial dislocations are

nucleated on a (111) leaving intrinsic stacking faults. The emission process results in a collapse of the high free volume structural unit from which the dislocation originally came. Further propagation of the emitted partial dislocation across the grain occurs for higher strain levels. This process is very similar to that observed by Spearot and coworkers in a study of CSL symmetrical tilt boundaries in Cu [6]. In that work, the "E" structural units were shown to be preferred sites for dislocation emission. These structural units are very similar to those observed to be the emission sites in our simulations in random boundaries. Our results therefore suggest that the emission process from random tilt boundaries is quite similar to that observed for symmetrical tilt boundaries.

For both relaxation treatments studied, the basic dislocation emission process was similar, but differences in local structure configuration due to the different relaxation state exist. In particular, these differences affect the amount of dislocation emission observed for the two different relaxation states. Dislocation emission is harder for the grain boundaries that are in the more relaxed state. A comparison of dislocation emission for the same group of atoms in the two different relaxation conditions is seen in Figure 5. These results indicate that sites in the grain boundary that are not fully relaxed to lowest energy local configurations can aid dislocation emission. Figure 5 also shows that the dislocation emission process results in changes in the local structure of the grain boundary.

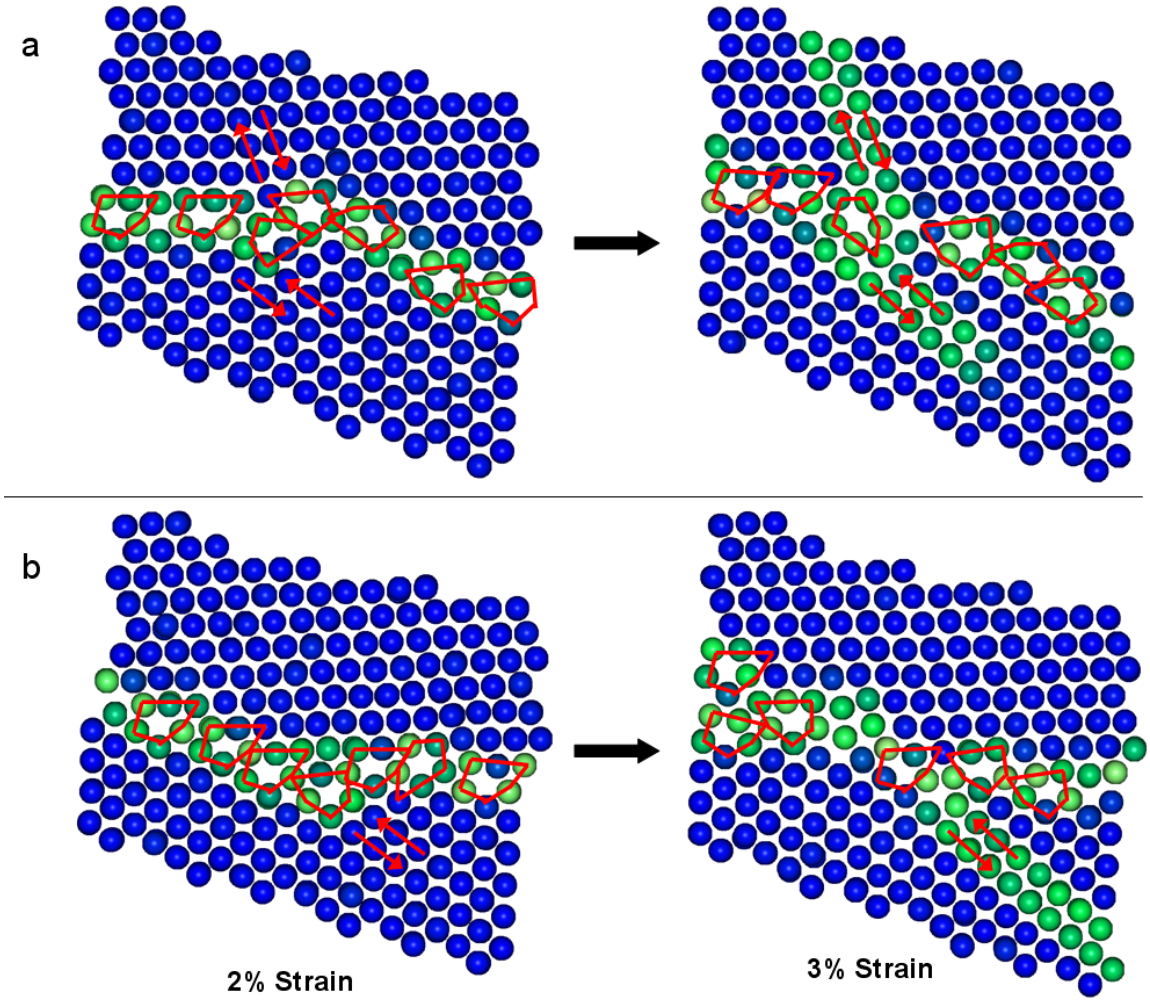

Figure 2.5 Detail of GB7-8 (RHA at 30.11°) showing dislocation emission with "E" structural units outlined in red. (a) High temperature relaxation treatment and (b) relaxed at 300K.

In addition to differences in dislocation emission, we also observe GB sliding in both of the samples, slightly more in the RT relaxed sample compared to the HT relaxed sample. This mostly occurs in boundaries that are oriented with respect to the tensile axis so that the adjacent grains form a shear component (i.e away from perpendicular.). No GB sliding was observed in RLA boundaries. An example of the extent of sliding between the two relaxation states can be seen in Figure 6.

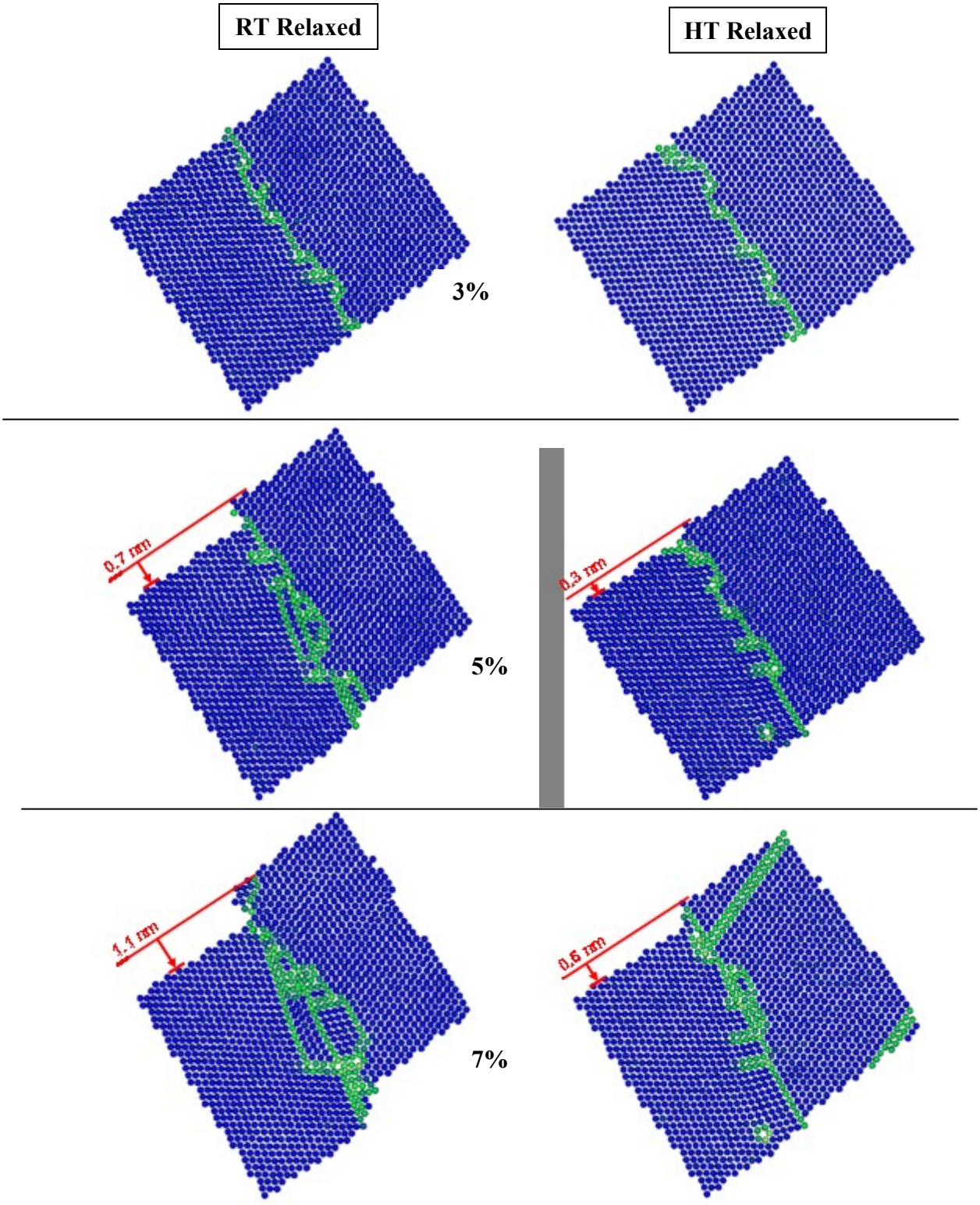

Figure 2.6 Detail of GB4-8 illustrating grain boundary sliding from 3% to 7% strain for both of the relaxed samples. The RT relaxed sample is shown on the left, HT relaxed sample shown on the right. The amount of relative sliding is shown in red.

The difference in the relaxation state of the digital sample boundaries also played a vital role in the overall mechanical behavior response. This is illustrated in Figure 7 where the samples exhibit similar deformation behavior up to about 3% strain and thereon deviate significantly. The high temperature (HT) relaxed sample experiences hardening, while the room temperature (RT) relaxed sample deforms with no apparent strengthening. This is to be expected if the overall dislocation emission process is harder in the sample where the boundaries are in a more relaxed, lower energy configuration.

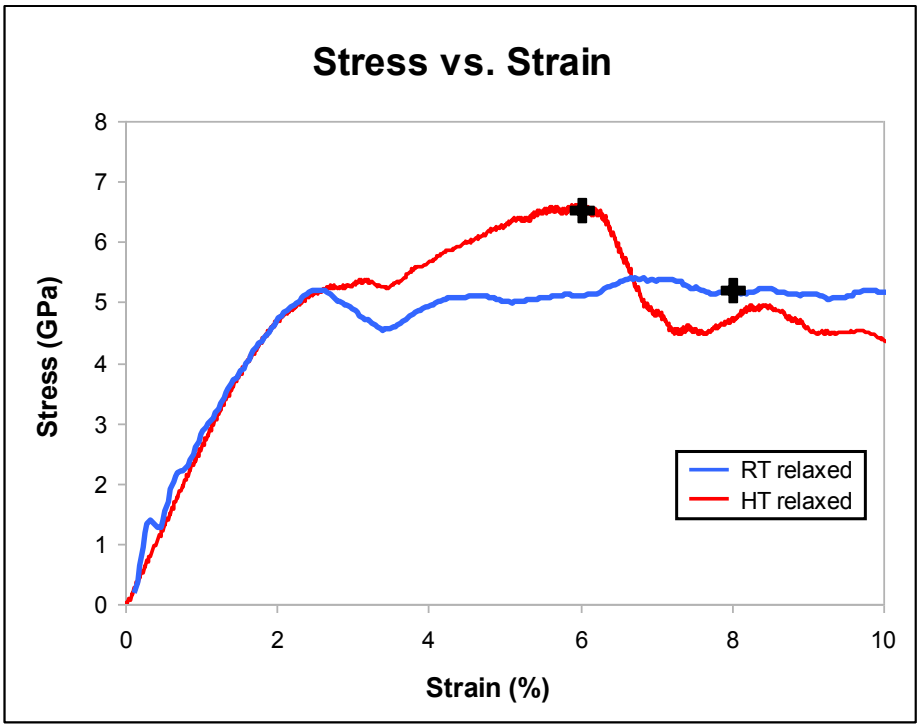

Figure 2.7 Stress-Strain curves for the sample relaxed at high temperature (HT) and at 300K (RT). The black "+" indicates the point of crack formation.

2.4.5 Effects of plastic deformation on the potential GB energy

The plastic deformation process of the samples through dislocation emission affects the local structure of the grain boundaries. Because structure is often correlated to energy, we

studied the grain boundary energy after varying amounts of deformation. Figure 8 shows the average GB energy dependence on the overall strain level for a group of nine boundaries in both relaxation states. For RT relaxed boundaries, the average excess grain boundary energy significantly decreases as the strain level increases. For HT relaxed boundaries, the average excess GB energy remains approximately constant as the strain level increases. This significant difference in the potential interfacial energy response to deformation can be interpreted as due to the dislocation emission from the local regions that are not in a fully relaxed state as well as GB sliding in the RT sample. This process changes the structure of the boundary to achieve a lower energy state. It is interesting to note that the boundaries that are less relaxed, through increased response to deformation, are able to achieve a lower energy state at higher deformation levels.

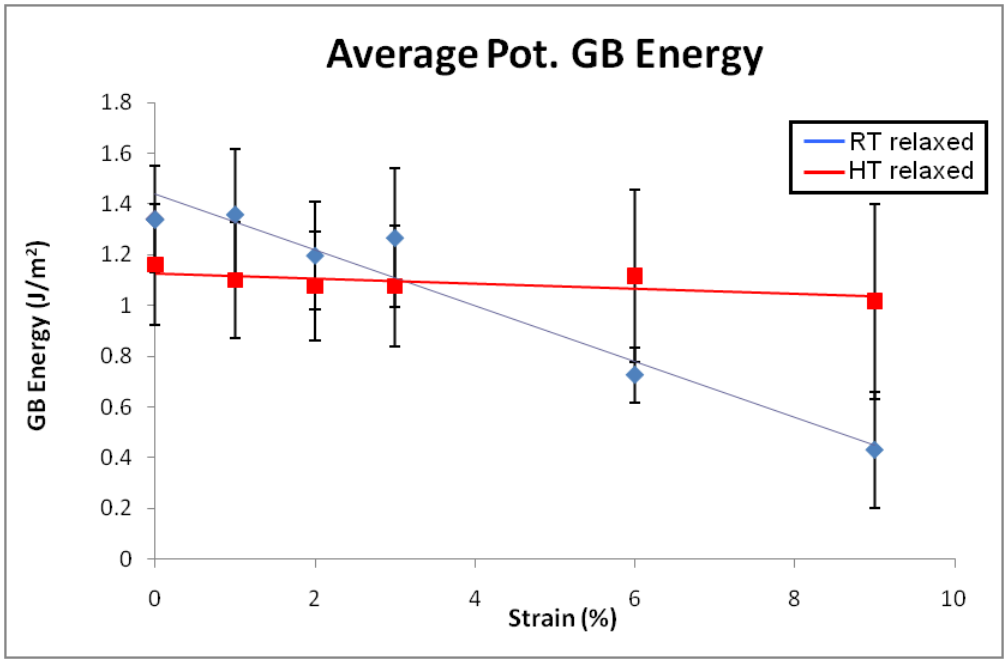

Figure 2.8 Plot of the average excess potential grain boundary energy versus strain for nine boundaries using two different relaxation treatments for the sample.

We then analyzed the energy response separately for the different types of boundaries under the two different relaxation treatments. The results can be seen in Figure 9. For both relaxation treatments, the RLA boundaries show a similar decrease in excess potential energy with increasing strain. The RHA boundaries exhibited the greatest difference in behavior caused by the different relaxation state. The RT relaxed boundaries decreased significantly with strain and the HT relaxed boundaries increased only slightly and/or remained approximately the same. The two Σ3 boundaries with GB planes near (112), GB2-5 and GB4-6, behaved similarly for both RT and HT, while the other Σ3, GB3-5, behaved very differently depending on the relaxation state.

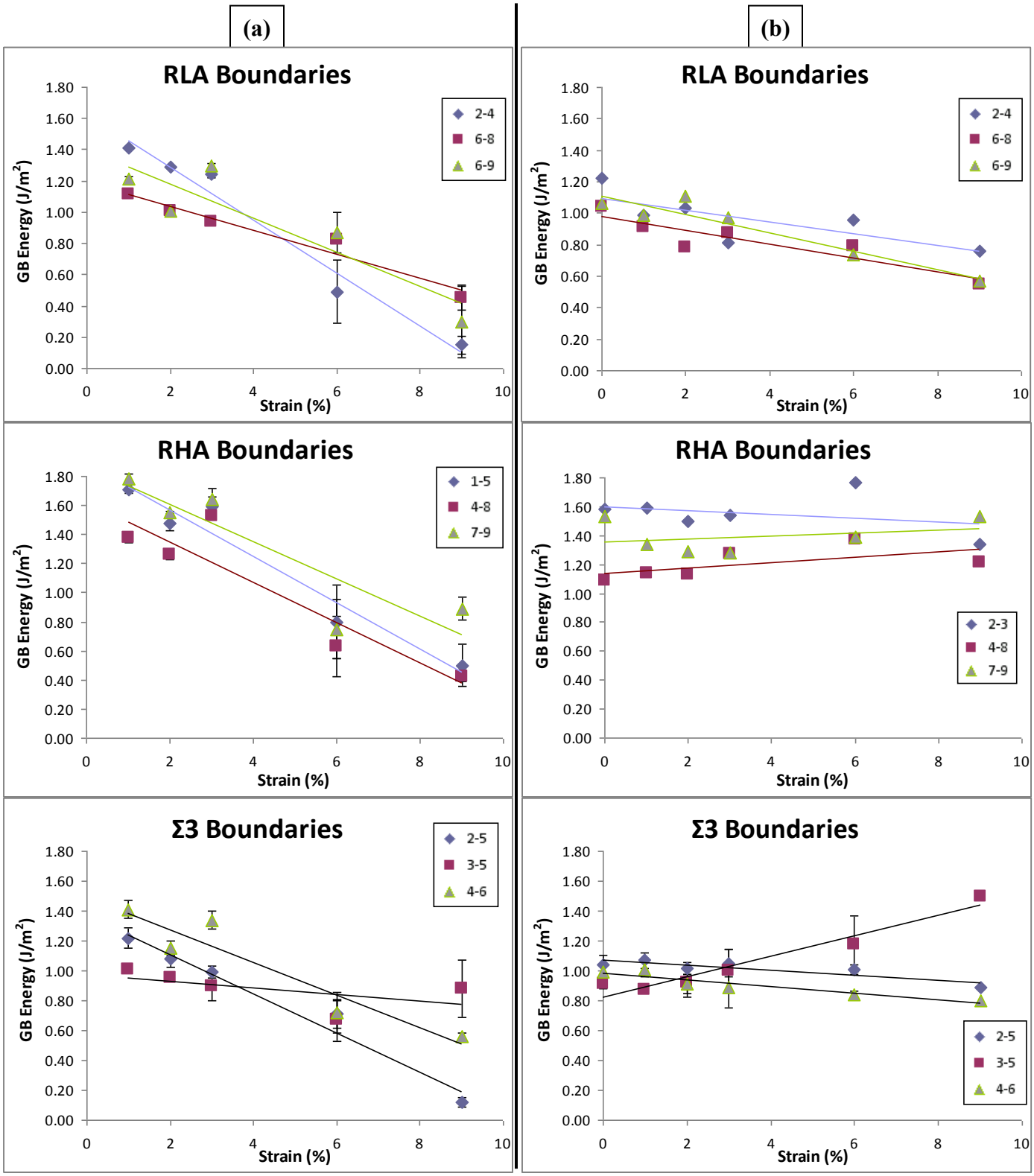

Figure 2.9 Plots of the excess grain boundary energy versus strain for the three different GB types in a side-by-side comparison between (a) RT relaxation on the left and (b) HT relaxation on the right.

2.4.6 Correlation of GB excess volume and potential GB energy

Figure 5 shows the emission of dislocations for areas in the grain boundary that contain high free volume. After the emission process, the free volume containing structural unit collapses, indicating a possible reduction in free volume in the GB. The work of Spearot in [6] confirms this mechanism with nanoporosity measurements [26] before and after partial dislocation emission. We used the coordination number instead as a relative indication of the amount of free volume based on the number of nearest neighbors per atom where CN=12 corresponds to a perfect lattice atom and the lowest amount of free volume. Due to the size of our boundary selection widths, the average GB coordination number was mitigated by the presence extra atoms, so we looked at just those atoms whose CN was less than 12 and divided by the area of the interface. The dependence of the average CN<12 as a function of strain can be seen in Figure 10. The RT relaxed sample decreases considerably from 1% to 9% strain, while the HT relaxed sample decreases slightly. Also, the HT sample is initially at a considerably lower average CN<12 than the RT sample. These results are consistent with those for the average GB potential energy as a function of strain suggesting a correlation between the two.

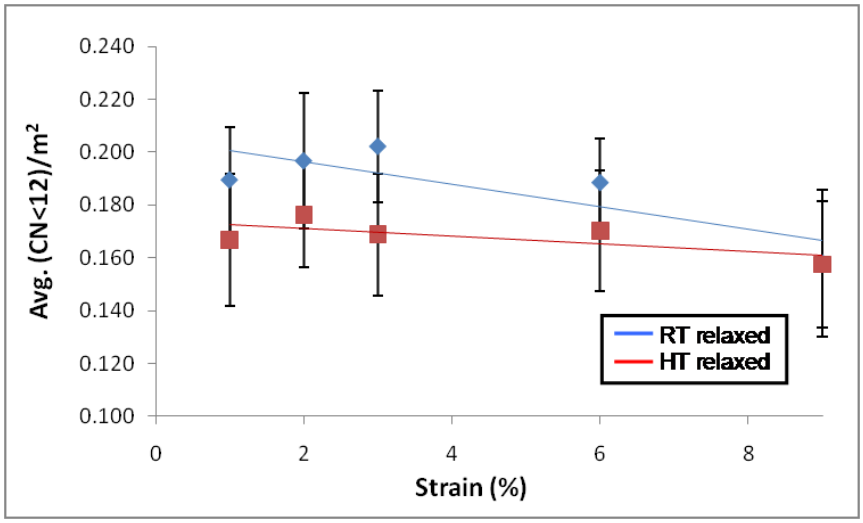

Figure 2.10 Plot of the average GB coordination number less than 12 per m^2 as a function of strain using two different relaxation treatments for the sample.

2.5 Discussion

The close similarities in the energy trends in Figure 2 between random and perfectly symmetrical tilt boundaries suggests that FCC polycrystalline metals behave similar in regards to grain boundary energy with misorientation angle. A more thorough study of grain boundary energies in pure Ni would have to be performed on a computer generated sample with a higher number of CSL boundaries, specifically Σ3, before this could be fully concluded. This would also better represent the higher ratios of Σ3 boundaries that are typically observed. The similarity in energy behavior also suggests that the grain boundary plane has a small effect on energy, and misorientation plays more of a vital role. Other sources report that the GB plane instead has a significant effect on energy and structure [2, 9, 27]. Although, this may be due to the fact that other works take into account the twist of the GB plane where our digital sample contains only pure tilt GB's.

For the random boundaries, the potential GB energy varied along the length of the boundary indicating local structure differences in the grain boundary as opposed to the same boundary structure throughout the entire GB as typically seen in symmetrical tilt boundaries. A closer look revealed that the middle region of the boundary usually had a lower E_{gb} than near the edges where the triple junctions likely lend to the increased energy. Also, the excess potential energy increased as the sample temperature increased due to the contributions from thermal energy. The increase corresponds to the balance in excess free energy and excess entropy where a simple equation would look something like E = G+TS with E as the potential energy, G as the free energy, and S as the entropy. The calculation of free energy would show a decrease with increasing temperature with additional increase in entropy [25, 28]. Figure 4 shows a graph of

excess GB potential energy with temperature in which the slopes of the lines are on the order of the ideal gas constant R ranging from 7 to 14 J/K.

The deformation process present in our sample occurs largely through the emission of partial dislocations from the random tilt grain boundaries, leading to plastic deformation as the strain progresses. Previous works show that the GB structure undergoes significant local change as a result of dislocation emission [6, 13]. In the simulation of <110> symmetric copper tilt grain boundaries, Spearot shows the lattice shift in boundary atoms resulting in the collapse of free volume at the interface during dislocation emission. As a relative measure of GB free volume, the average CN<12 was observed to decrease with deformation, which confirmed the dislocation emission process. The structure-energy work of Wolf showed good correlation between the coordination number and the GB energy [2]. This means the reduction in free volume as a dislocation is emitted will lead to a higher coordination number resulting in a decrease in energy at the interface. Therefore, the reduction of excess potential GB energy in the sample is a result of free volume reduction as dislocations are emitted from the boundaries.

The deformation response and GB energies were significantly affected by the relaxation temperature. In the HT sample, the GB's were initially in a much lower energy configuration and lower free volume, which made dislocation emission much harder. Also, GB sliding was an additional deformation mechanism in the RT sample, allowing it to achieve lower GB energies with higher deformation levels. This significant difference in deformation mechanism accounts for the strengthening seen in Figure 6 as mentioned in the work of Vo, et al. [18]. For both samples, the RLA boundaries decreased in energy because they disappeared with strain. The HT random high-angle boundaries did not decrease with increasing strain, suggesting that GB sliding was the primary mechanism for energy decrease for RHA boundaries in the RT relaxed sample.

2.6 Conclusions

Molecular dynamics simulations were used to analyze the excess potential energy behavior of random <110> tilt grain boundaries as a function of grain misorientation, temperature, and plastic deformation. The first major result is that the random tilt boundaries of Ni were found to follow the same trend of excess GB energy dependence on misorientation angle compared to the symmetric tilt boundaries of Al, suggesting a small effect on energy from the boundary plane. This has been disputed in other works arguing that GB plane plays a vital role in interfacial energy [2, 9, 27]. In addition, the excess energy along the length of the random boundaries varied due to differences in local structure, which is not observed in symmetric boundaries. The excess GB potential energy increases with increasing temperature, while the excess free energy decreases.

Deformation in the sample occurs mostly through the emission of dislocations from the random tilt boundaries and is similar to the process that occurs in symmetrical tilt boundaries. This process causes changes in the local boundary structure from the collapsing of structural units and shifting of nearby atoms resulting in changes in excess potential boundary energy and mechanical response. The high temperature relaxed sample was found to strengthen due to forced dislocation emission, whereas the room temperature relaxed sample deformed with no strengthening due to the added mechanism of GB sliding. The RT and HT relaxed boundaries behaved similar in regards to decrease in energy with increasing strain except for the HT random high-angle boundaries, which showed small increases in energy. This suggests that RHA boundaries do not conform to lower energy states when the primary deformation mechanism is dislocation emission.

2.7 Acknowledgements

This work was supported by the Department of Energy, Office of Basic Energy Sciences, under grant DE-FG02-08ER46525. The work presented here is also a continuation of previous research on dislocation behavior and structure evolution under deformation by Diana Farkas and Laura Patrick.

2.8 References

1. Sutton, A. and R. Balluffi, *Interfaces in Crystalline Materials*. 1995, Oxford: Clarendon Press.
2. Wolf, D., *Structure-energy correlation for grain-boundaries in fcc metals - 3. Symmetrical tilt boundaries* Acta Metallurgica Et Materialia, 1990. **38**(5): p. 781-790.
3. Tschopp, M.A., G.J. Tucker, and D.L. McDowell, *Structure and free volume of < 110 > symmetric tilt grain boundaries with the E structural unit.* Acta Materialia, 2007. **55**(11): p. 3959-3969.
4. Tschopp, M.A. and D.L. McDowell, *Asymmetric tilt grain boundary structure and energy in copper and aluminium.* Philosophical Magazine, 2007. **87**(25): p. 3871-3892.
5. Spearot, D.E. and D.L. McDowell, *Atomistic Modeling of Grain Boundaries and Dislocation Processes in Metallic Polycrystalline Materials.* Journal of Engineering Materials and Technology-Transactions of the Asme, 2009. **131**(4).
6. Spearot, D.E., *Evolution of the E structural unit during uniaxial and constrained tensile deformation.* Mechanics Research Communications, 2008. **35**(1-2): p. 81-88.
7. Schmidt, C., et al., *Theoretical and experimental investigations of structures and energies of Sigma = 3, 112 tilt grain boundaries in copper.* Philosophical Magazine a-Physics of Condensed Matter Structure Defects and Mechanical Properties, 1998. **77**(5): p. 1161-1184.
8. Rittner, J.D. and D.N. Seidman, *<110> symmetric tilt grain-boundary structures in fcc metals with low stacking-fault energies.* Physical Review B, 1996. **54**(10): p. 6999-7015.
9. Mishin, Y., M. Asta, and J. Li, *Atomistic modeling of interfaces and their impact on microstructure and properties.* Acta Materialia, 2010. **58**(4): p. 1117-1151.
10. Saylor, D.M., et al., *Distribution of grain boundaries in aluminum as a function of five macroscopic parameters.* Acta Materialia, 2004. **52**(12): p. 3649-3655.
11. Rohrer, G.S., et al., *The distribution of internal interfaces in polycrystals.* Zeitschrift Fur Metallkunde, 2004. **95**(4): p. 197-214.
12. Kim, C.S., A.D. Rollett, and G.S. Rohrer, *Grain boundary planes: New dimensions in the grain boundary character distribution.* Scripta Materialia, 2006. **54**(6): p. 1005-1009.
13. Farkas, D. and L. Patrick, *Tensile deformation of fcc Ni as described by an EAM potential.* Philosophical Magazine, 2009. **89**(34-36): p. 3435-3450.
14. Mishin, Y., et al., *Interatomic potentials for monoatomic metals from experimental data and ab initio calculations.* Physical Review B, 1999. **59**(5): p. 3393-3407.
15. Plimpton, S., *Fast Parallel Algorithms for Short-Range Molecular Dynamics.* Journal of Computational Physics, 1995. **117**(1): p. 1-19.

16. Farkas, D. and W.A. Curtin, *Plastic deformation mechanisms in nanocrystalline columnar grain structures.* Materials Science and Engineering a-Structural Materials Properties Microstructure and Processing, 2005. **412**(1-2): p. 316-322.
17. Lee, B.J. and S.H. Choi, *Computation of grain boundary energies.* Modelling and Simulation in Materials Science and Engineering, 2004. **12**(4): p. 621-632.
18. Vo, N.Q., et al., *Limits of hardness at the nanoscale: Molecular dynamics simulations.* Physical Review B, 2008. **78**(24).
19. Kelchner, C.L., S.J. Plimpton, and J.C. Hamilton, *Dislocation nucleation and defect structure during surface indentation.* Physical Review B, 1998. **58**(17): p. 11085-11088.
20. Brandon, D., Acta Metall., 1966. **14**.
21. Randle, V., *An investigation of grain-boundary plane crystallography in polycrystalline nickel.* Journal of Materials Science, 1995. **30**(16): p. 3983-3988.
22. Otsuki, A. and M. Mizuno, *Grain Boundary Structure and Related Phenomena.* Trans. Jpn Inst. Metals, 1986. **27**.
23. Hasson, G. and C. Goux, *Interfacial energies of tilt boundaries in aluminum - Experimental and theoretical determination.* Scripta Metallurgica, 1971. **5**.
24. Hashimoto, M., et al., *Thermodynamic Properties of Coincidence Boundaries in Aluminum.* Acta Metallurgica, 1981. **29**(4): p. 617-626.
25. Artemyev, A. and L. Fionova, *Grain Boundaries in Metals and Semiconductors*. Les Editions de Physique. 1993, France: Europe Media Duplication S.A.
26. Spearot, D.E., et al., *Tensile strength of < 100 > and < 110 > tilt bicrystal copper interfaces.* Acta Materialia, 2007. **55**(2): p. 705-714.
27. Randle, V., *The role of the grain boundary plane in cubic polycrystals.* Acta Materialia, 1998. **46**(5): p. 1459-1480.
28. Lutsko, J.F., D. Wolf, and S. Yip, *Molecular-dynamics calculation of free-energy.* Journal of Chemical Physics, 1988. **88**(10): p. 6525-6528.

Chapter 3: Plastic Deformation of Random Grain Boundaries in a Thin-film

3.1 Abstract

Molecular dynamics simulations are used to study the plastic deformation behavior of a computer-generated thin-film sample with free-surfaces consisting of FCC polycrystalline Ni. The thin-film was deformed in the X- and Y- direction, and a side-by-side comparison of the deformation response was made. The similarity in dislocation emission behavior was examined between a columnar grain sample and the thin-film sample. An additional deformation mechanism was observed as an effect from the thin-film and sample thickness. Furthermore, failure of the thin-film sample was briefly discussed.

3.2 Introduction

Deformation response in a metal has been linked to the local boundary structure through the emission of dislocations from random tilt boundaries [1-3]. Samples created with a columnar grain structure and tilt boundaries utilize periodic boundary conditions in all directions to increase the simulation cell size and aid in the visualization of the sample during deformation. While this is useful for increasing the mean grain size out of the nano-scale, the forced periodic boundary condition in the columnar direction will restrict dislocations to only form on certain slip systems [1]. A 3D grain structure will more accurately model the materials response to loading and create a larger assortment of grain boundaries such as those consisting of tilt and twist characteristic. Due to computational limitations associated with the massive number of atoms in a fully 3D model, a thin-film sample with free surfaces can be used instead to achieve a 3D grain structure with large enough grains and avoid nano-size effects.

This paper studies the plastic deformation behavior of a computer-generated thin-film sample with free-surfaces consisting of FCC polycrystalline Ni. The initial sample is relaxed via high temperature equilibration and then deformed in both the X- and Y-direction at 300K for comparison of deformation response and role of the GB's between the two tensile directions. The simulations are modeled using molecular dynamics via the embedded atom method.

3.3 Methodology

The thin-film sample was generated using a Voronoi construction [4] with specified Euler's angles, grain centers, and thickness with free surfaces in Z and periodic boundary conditions in X and Y. The 3D grain configuration was modeled from an austenitic steel sample studied at the University of Michigan [5] and contained 8 grains that were approximately 20nm in diameter and 3nm thick. The resulting thin-film had a total of 24 grain boundaries, all of random type including low-angle, high-angle, and Σ3.

The program used for the standard molecular dynamics simulation was LAMMPS [6] with the interatomic potential of Mishin et al for Ni [7]. The grain boundaries in the sample were relaxed via a high temperature annealing treatment by heating to 1200K and cooling back to 300K in 450ps to help them find their lowest energy configuration. The sample was then tensely deformed separately in both the X- and Y-direction at a rate of 3.3×10^{8} s^{-1} up to 15% at 300K, and data for individual atoms was recorded every 1% strain including atomic position, centrosymmetry [8], and stress. The temperature was controlled using a Nose-Hoover thermostat, and the pressure was controlled using a Nose-Hoover barostat to keep the pressure zero in the direction perpendicular to the tensile axes except for in Z.

Due to the thin-film configuration, a 6Å slice was taken perpendicular to the Z-direction through the center of the sample to remove any interference from the free surface in the visualizations. A slice of the sample and grain layout can be seen in Figure 1.

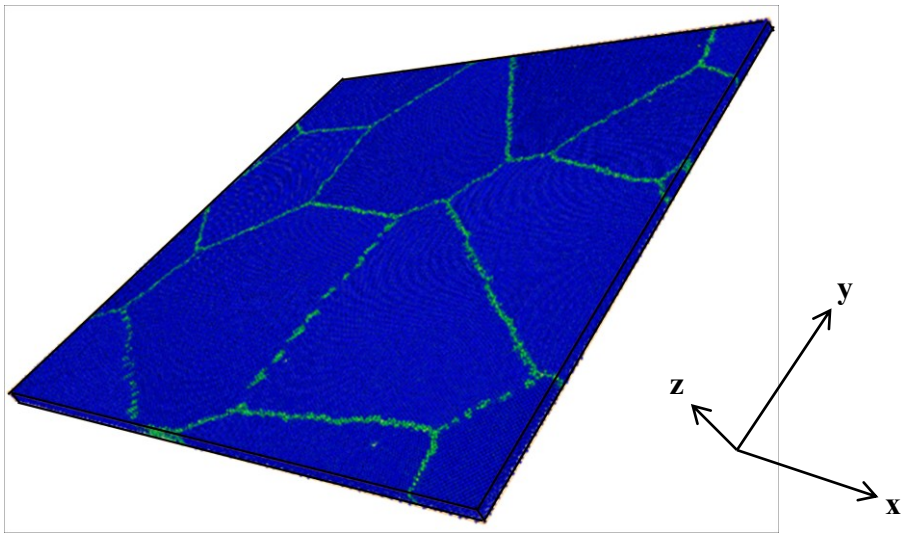

Figure 3.1 Thin-film sample configuration with a thickness of 3nm. This sample contains 8 grains, approx. 20nm in diameter with a total of 24 GB's.

3.4 Results and Discussion

3.4.1 Deformation behavior of thin-film sample

Figure 2 shows the stress-strain behavior of the thin-film sample deformed in both the X- and Y-direction. The tensile behavior is different as the loading direction is changed due to the limited number of grain boundaries contained in the sample and the varying response of each to the loading [3]. This difference is notably seen after 3% strain where the sample deformed in the X requires a lower stress input thereon to achieve the same deformation as in the Y.

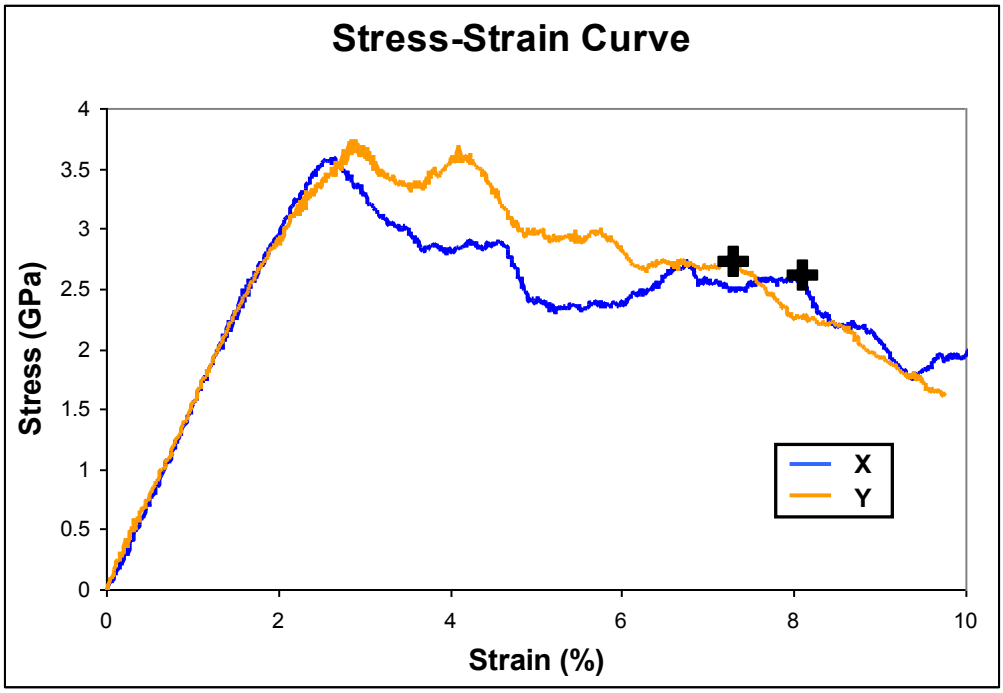

Figure 3.2 Stress versus Strain curve for the thin-film sample deformed in both the X and Y direction. The black "+" indicates the point of crack formation.

To obtain further explanation on the stress-strain behavior, the sequence of tensile deformation at 3, 5, and 7% is shown in Figure 3. Heterogeneous displacement maps were created by normalizing the deformed atomic coordinates at a specific strain level to the undeformed atomic positions. The difference between the two results in deformation maps used to help visualize the strain gradients and slipped areas in the material. In combination with atoms filtered by a centrosymmetry parameter [8] greater than 3, the grain boundaries and stacking faults were also visualized to generate a side-by-side comparison of the complete deformation process. As seen in Figure 3, similar grain boundaries act as dislocation emission sites for both tensile directions, but the dislocations are ejected into different grains. This demonstrates two important behavior mechanisms: the effect of the boundary structure on dislocation emission, and emission direction based on the grain dependence of available slip systems for that particular Schmid factor. Using GB2-3 as an example of this behavior, grain 2

experiences significant dislocation activity when deformed in the Y-direction and zero activity in the X-direction; however, grain 3 experiences no dislocation activity when deformed in the Y-direction and considerable activity for the X-direction. This mechanism is similar to that observed in a sample of <110> tilt boundaries with columnar grains [3].

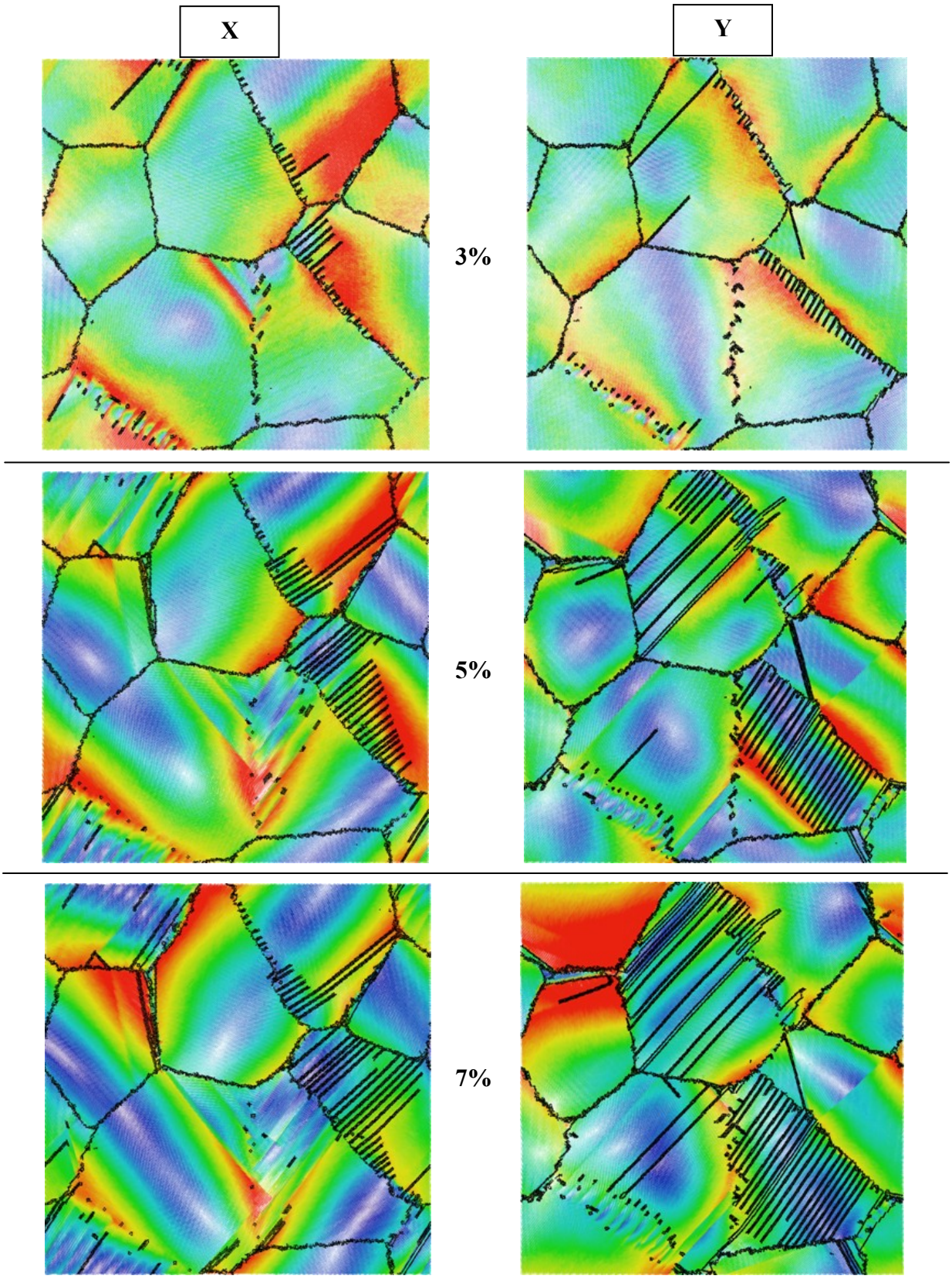

Figure 3.3 Heterogeneous deformation maps for thin-film sample. Strain levels of 3, 5, and 7% in both directions are shown. The color map used is from blue to red where red indicates heterogeneous displacements up to 0.25, 0.6, and 0.8 nm. Atoms with centrosymmetry parameter greater than 3 are in black.

Figure 4 shows the evolution of the grain boundaries as a result of dislocation emission up to 7% strain. The red atoms represent the initial boundary position, and the black atoms represent the GB position and stacking faults after deformation. One boundary of interest is GB2-3, a Σ3, as it moves considerably from its initial position showing an increased response to load. As seen between the two tensile directions, the GB moves mostly perpendicular and opposite of the emitted dislocation. When deformed in the Y-direction, the boundary generates more dislocations and moves significantly more than when deformed in the X-direction, which suggests that the amount of GB movement is a function of emission. This behavior is only observed to occur in Σ3 boundaries and can be seen again in GB7-8. For this boundary deformed in the Y-direction, however, little movement occurs indicating an additional factor, possibly related to the GB and grain orientation.

Interesting GB evolution also occurred in the low-angle boundary GB1-6. As the deformation level is increased in the X-direction, dislocations are emitted completely across grain 1 and the grain boundary starts to disappear. By 7% strain, most of the original GB has disappeared. Deformation in the Y-direction leads to a much different response. Instead of the boundary disappearing with increased deformation, the arrangement of dislocations constituting that boundary uniformly glides into grain 6, which results in the movement of the low-angle boundary with little annihilation from dislocation emittance. The difference can be attributed to the change in preferred slip system from the X- to the Y-tensile direction, but with dislocation movement being more difficult in grain 6.

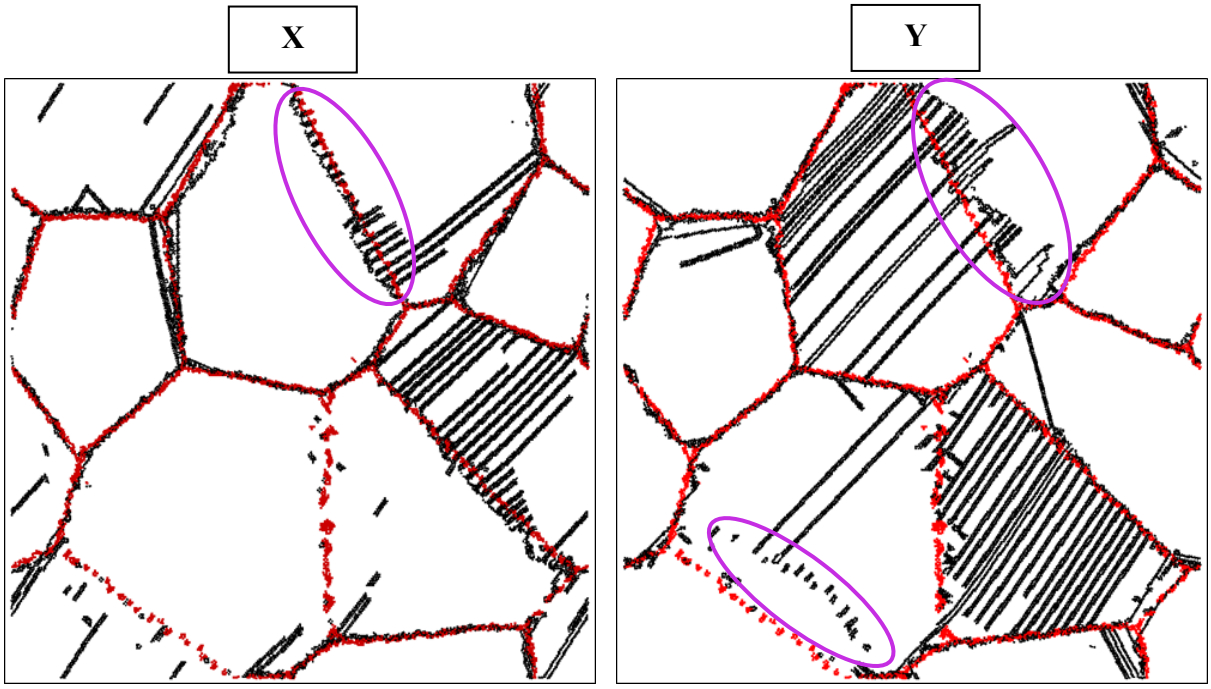

Figure 3.4 Thin-film sample at 7% strain for both tensile directions illustrating GB movement. Only atoms with centrosymmetry>3 are shown where black indicates GB positions at the current strain and red is the initial boundary positions at 0% strain. Areas of significant movement are outlined in pink.

In addition to dislocation emittance and travel as a means of deformation, the thin-film sample also experienced a significant amount of GB sliding, thus allowing the grains to shear parallel to the boundary. Sliding was observed to occur in 9 of the 24 boundaries for both tensile directions. It is important to note that little to no GB sliding should have occurred since the sample's grain boundaries were relaxed using a high temperature annealing treatment [2, 9]. Figure 5 shows an example of GB sliding representative of that occurring in the other boundaries of the sample. While sliding occurred in 5 of the same boundaries, the other 4 were unique to the tensile direction. Interestingly, GB sliding that was common to both deformation directions lead to shearing of the grains in opposite directions. Also, the direction of grain shear at the boundary was dependent on the angle of the GB with respect to the tensile axis; this is due to the elongating of the grains during deformation where the GB's try to align with the tensile direction. The 3nm thickness of the sample was the source of the GB sliding due to thin-film effects related to the glide of dislocations to the free surface [10]. Repetitive termination of

dislocations at the free surface lead to the thin-film "warping", which resulted in increased stress anisotropy, specifically shear stresses.

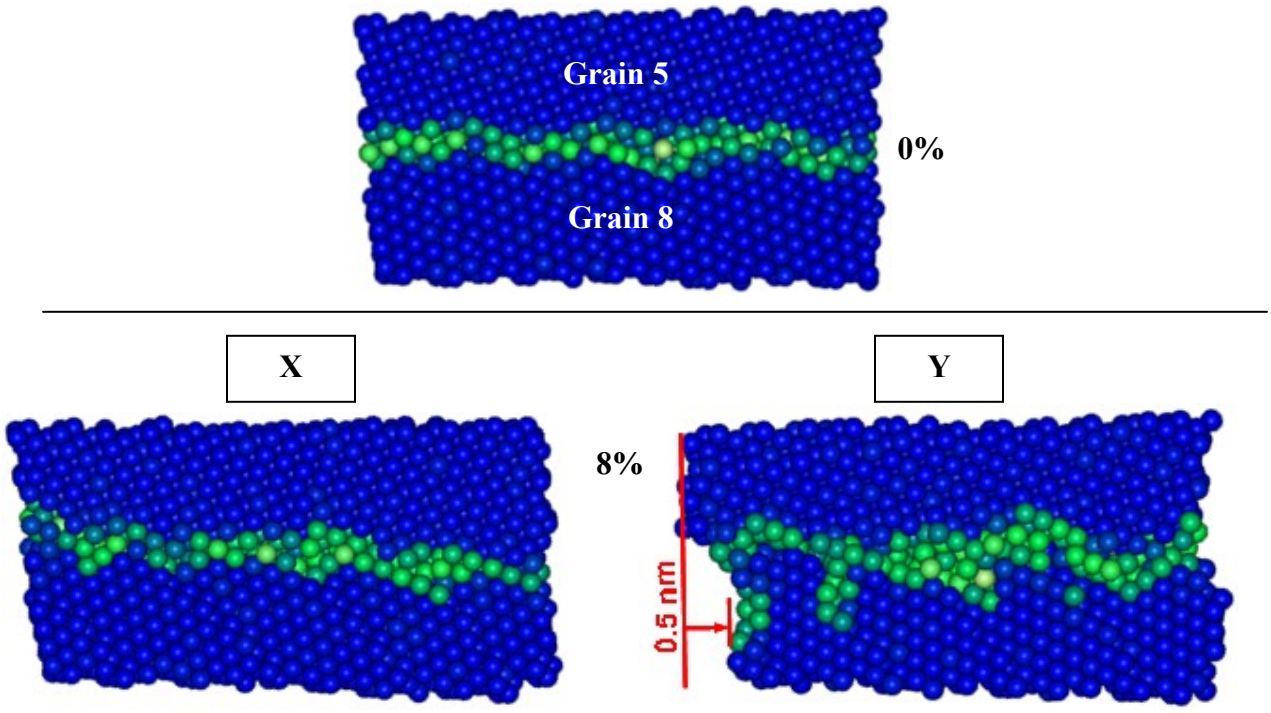

Figure 3.5 Detail of GB5-8 at 0% and 8% strain in both directions illustrating grain boundary sliding for the y-direction. Atoms colored with the centrosymmetry parameter from 0 (blue) to 12 (yellow). The amount of sliding, in nm, is calculated in red.

3.4.2 Failure of sample

After significant plastic deformation, the sample formed a crack in the grain boundary, followed by steady crack growth with continual deformation. This occurred at 8% strain in GB2-5 for X and 7% strain in GB1-5 for Y. Figure 6 shows the process of crack formation in the X tensile direction with a view from the top and a cross-section through the thickness of the thin-film. The blue atoms indicate atoms with the highest amount of surrounding symmetry (i.e. perfect lattice atom), and the yellow atoms indicate the lowest amount of surrounding symmetry (i.e. free surface atom). At 6% strain, the sample is beginning to thin above and below the boundary. At 8% strain, the increased deformation has caused much more thinning, resulting in

small cracks forming between the two grains. This failure behavior at the atomic scale is similar to that which occurs in the microscopic and macroscopic scale for bulk, ductile metals.

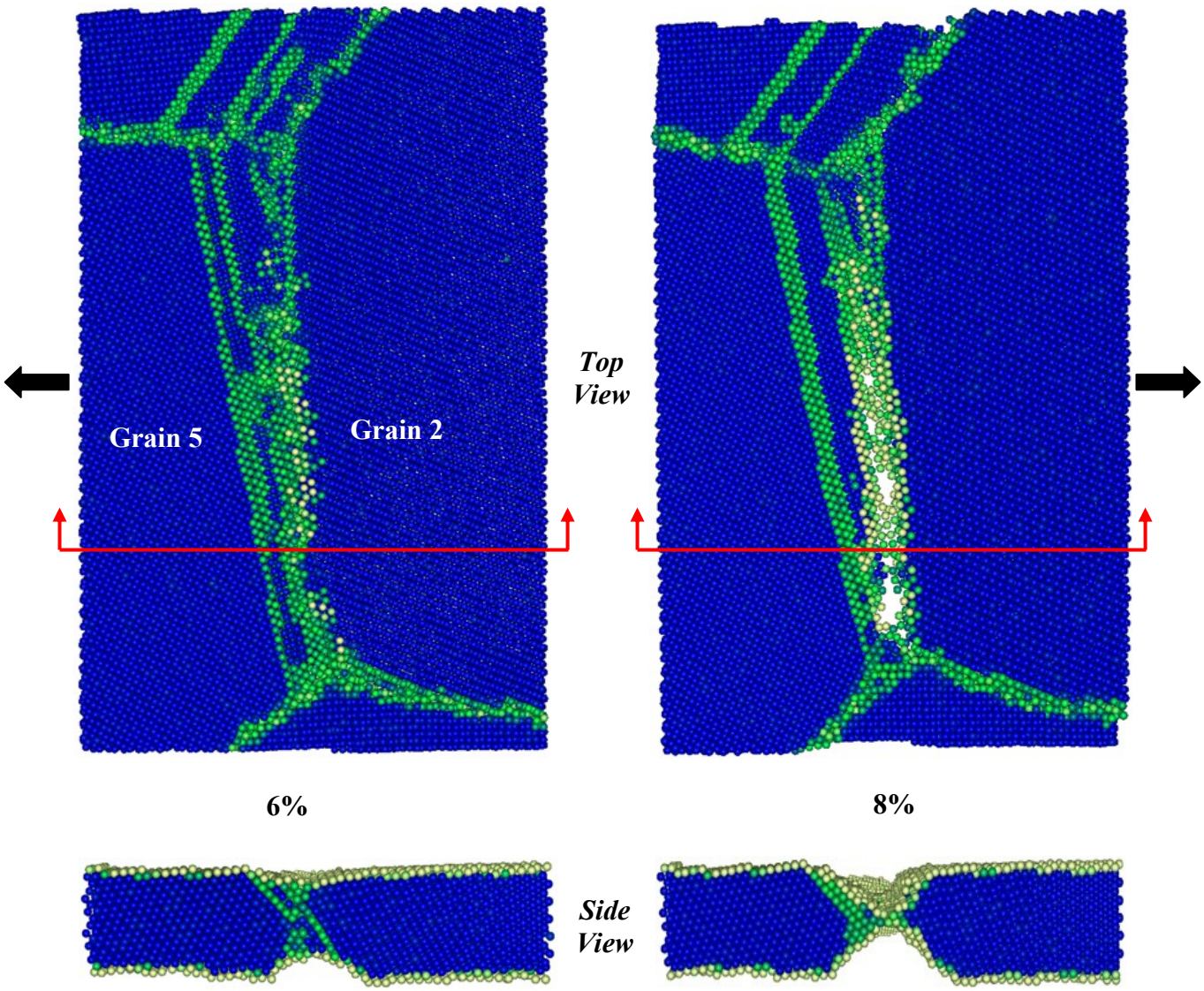

Figure 3.6 Crack formation in GB2-5 for the sample deformed in the X-direction. The bottom pictures show the full thickness cross-section of the thin-film indicated by the red arrows. Atoms colored with the centrosymmetry parameter from 0 (blue) to 12 (yellow).

3.5 Conclusion

Plastic deformation of a thin-film sample with 3D configuration revealed dislocation emission behavior consistent with that of a columnar grain sample with 2D configuration in regards to dependence on local grain boundary structure and Schmid factor. The type of boundary, directly related to its structure, resulted in different loading response. Even after relaxing the initial GB's with a high temperature annealing treatment, the sample experienced GB sliding in approximately a third of all the boundaries during deformation. The sliding was a result of thin-film effects coupled with the small sample thickness. After large amounts of deformation, the sample failure occurred via thinning at the GB and formation of small cracks in the thinned region between grains.

3.6 References

1. Spearot, D.E. and D.L. McDowell, *Atomistic Modeling of Grain Boundaries and Dislocation Processes in Metallic Polycrystalline Materials.* Journal of Engineering Materials and Technology-Transactions of the Asme, 2009. **131**(4).
2. Floyd, N.P., *Chapter 2: Energetics and Plastic Deformation Behavior of <110> Random Tilt Grain Boundaries.* Thesis, 2010.
3. Farkas, D. and L. Patrick, *Tensile deformation of fcc Ni as described by an EAM potential.* Philosophical Magazine, 2009. **89**(34-36): p. 3435-3450.
4. Farkas, D. and W.A. Curtin, *Plastic deformation mechanisms in nanocrystalline columnar grain structures.* Materials Science and Engineering a-Structural Materials Properties Microstructure and Processing, 2005. **412**(1-2): p. 316-322.
5. *13Cr15Ni Austenitic Steel Grain Clusters for Use in Strain Modeling.* via Private Communication, 2009.
6. Plimpton, S., *Fast Parallel Algorithms for Short-Range Molecular Dynamics.* Journal of Computational Physics, 1995. **117**(1): p. 1-19.
7. Mishin, Y., et al., *Interatomic potentials for monoatomic metals from experimental data and ab initio calculations.* Physical Review B, 1999. **59**(5): p. 3393-3407.
8. Kelchner, C.L., S.J. Plimpton, and J.C. Hamilton, *Dislocation nucleation and defect structure during surface indentation.* Physical Review B, 1998. **58**(17): p. 11085-11088.
9. Vo, N.Q., et al., *Limits of hardness at the nanoscale: Molecular dynamics simulations.* Physical Review B, 2008. **78**(24).
10. Wang, Z.Q., et al., *Dislocation motion in thin Cu foils: a comparison between computer simulations and experiment.* Acta Materialia, 2004. **52**(6): p. 1535-1542.

Chapter 4: Cracking Behavior of Random Grain Boundaries

4.1 Abstract

Molecular dynamics simulations are use to study the intergranular cracking behavior of model FCC polycrystalline samples. These samples include both columnar grain configurations with random boundaries as well as a sample that has a thin-film configuration with grain and GB orientations modeled after an experimental sample made of austenitic steel. Various factors for the cracked boundaries are analyzed such as GB type, crack orientation, etc. and a general trend in the simulated cracking behavior is made for all of the samples. We further discuss the comparison of the thin-film model sample and the experimental sample results.

4.2 Introduction

Grain boundaries have been shown to play a critical role in the deformation of metals, specifically those whose grain sizes are less than 100μm. While deformation is important for a material being used in service for any application, the fracture behavior is even more important in terms of cost, safety, and time of repair. Experiments and simulations have been performed on metal samples to understand the mechanism of crack growth; however, little work has been done to address the issue of the initial crack initiation. Simulation work by Cao and Wei [1] reveal intergranular fracture as the result of the coalescence of nanovoids by the breaking of atomic bonds at grain boundaries and triple junctions. The variables affecting crack initiation in the boundary, which are the most essential elements in understanding intergranular fracture, still remain to be determined.

The focus of this paper is on the cracking behavior of random grain boundaries and to qualitatively and quantitatively assess the possible factors affecting crack nucleation. Three

samples are utilized, each with varying grain configurations and boundaries, and deformed in the X- and Y-direction to make a cumulative cracking study. A total of 74 grain boundaries are present as possible sources of crack formation. The simulations are modeled using molecular dynamics via the embedded atom method. Various factors are used to make a general trend in crack behavior and compared with results from crack initiation in experimental austenitic steel samples[2].

4.3 Methodology

In order to study the general cracking behavior of GB's, multiple digital samples were created for comparison. The first sample, denoted "9g40n", has a grain and grain boundary network that was generated using a Voronoi construction [3] with random grain orientation and boundary misorientation angles tilted around the <110> axis such that all the boundaries are of only tilt characteristic. This digital sample contains 9 grains that are approximately 40nm in diameter and uses a 2D columnar grain structure with periodic boundary conditions in the x-, y-, and z-direction as shown in Figure 1a, similar to the sample in Farkas and Patrick [4] and Chapter 2 [5]. The periodic boundary conditions help eliminate the free surface effects. The second sample, denoted "TEM2D", was generated using the same Voronoi construction with columnar grains tilted around <110> and periodic boundary conditions in all directions, except with a grain layout identical to an experimental sample [6] shown in Figure 2. Due to limitations of the Voronoi construction, grains 6 and 10 of the experimental sample could not be reproduced. This digital sample contains 8 grains that are approximately 20nm in diameter. The third sample, denoted "TEM3D", was created to accurately model the same experimental sample [6], except with a 3D grain configuration. Voronoi construction was used to create a thin-film sample with identical grain and GB misorientations to the experimental sample. This digital

sample contains 8 grains that are approximately 20nm in diameter and 3nm thick with free surfaces in the z-direction and periodic boundary conditions in the other two; this sample is identical to the thin-film used in Chapter 3 [7]. There are a total of 73 grain boundaries between the three samples as described by random high-angle (RHA), random low-angle (RLA) and Σ3.

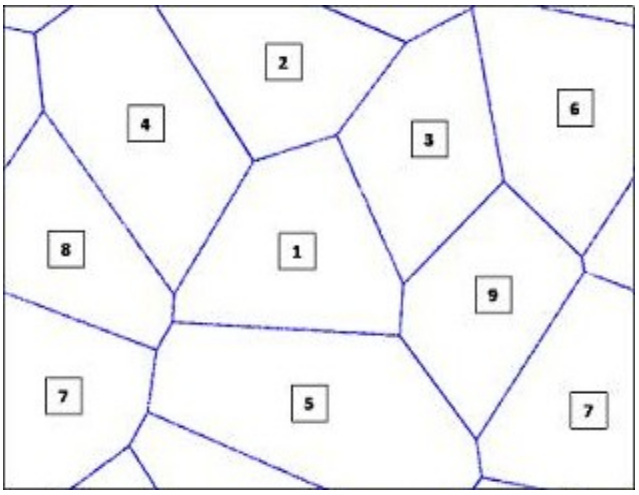

Figure 4.1 One sample configuration, 9g40n [4, 5], used for cracking analysis. This sample contains 9 grains, approx. 40nm in diameter with a total of 25 GB's.

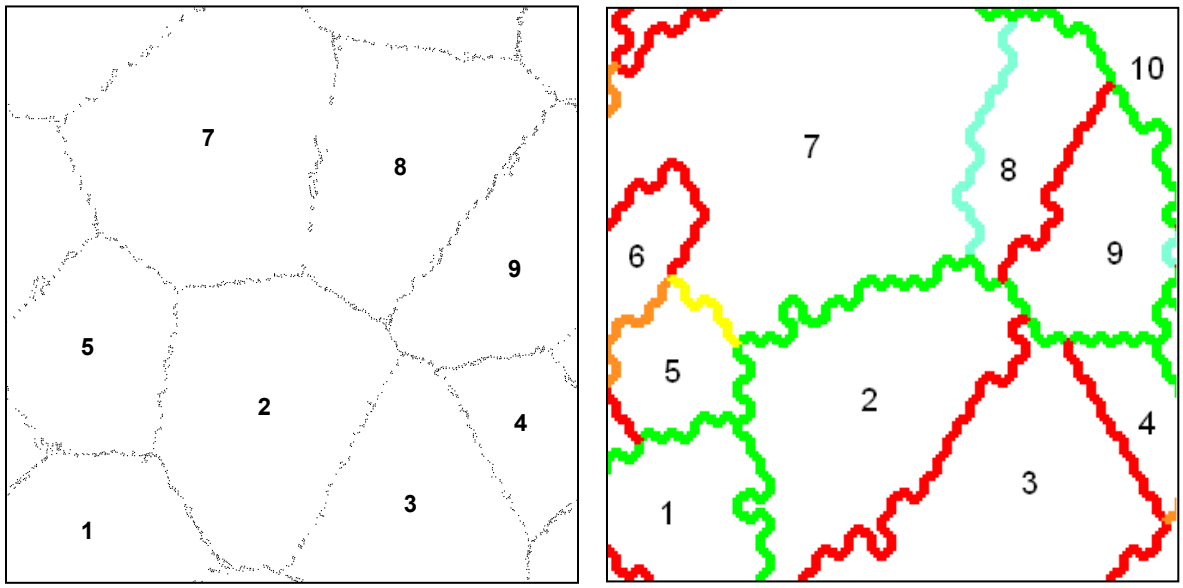

Figure 4.2 (a) Two sample configurations used for cracking analysis where TEM2D contains a columnar grain structure and TEM3D [7] contains a thin-film structure. These samples both contain 8 grains, approx. 20nm in diameter with 24 GB's. TEM3D was created to model (b) an experimental sample made of 13Cr15Ni austenitic steel [6].

The simulation code used for the standard molecular dynamics simulation is LAMMPS [8] using a Nose-Hoover thermostat and barostat with a well known interatomic potential of Mishin et al. for Ni [9]. The samples were tensely deformed in both the X- and Y-direction at a rate of $3.3x10^{8}$ s^{-1} up to 15% strain to obtain two series of data for each sample at room temperature. For the 9g40n and TEM2D sample, the pressure was kept at zero in the directions perpendicular to the tensile axis, but was allowed to vary in the z-direction of the TEM3D sample due to its free surface. Data for individual atoms was recorded every 1% strain including atomic position, centrosymmetry [10], potential energy, and stress to study multiple venues of cracking nucleation possibilities. The grain boundary energy calculated was that of the excess potential energy, and the measurement process is detailed in Chapter 2 [5]. The current study serves as a baseline for crack formation in an initially defect-free sample.

4.4 Results and Discussion

Because the exact cause of intergranular crack initiation is not well understood, a range of possible factors were examined in order to formulate a general trend in cracking behavior. The following sections examine these various factors; however, there could still be more possible factors responsible for crack formation. A total of 9 cracks were observed and studied.

4.4.1 Cracked boundary type

Only RHA boundaries were observed to crack in the nine cracked boundaries analyzed as seen in Figure 3. This data has not been normalized to the distribution of boundary types in the samples. RHA boundaries typically represented about 50% of the total boundary population in the three simulated samples. Changing this distribution may change the statistics; however, these numbers represent similar distributions seen in experimental austenitic steel samples [2].

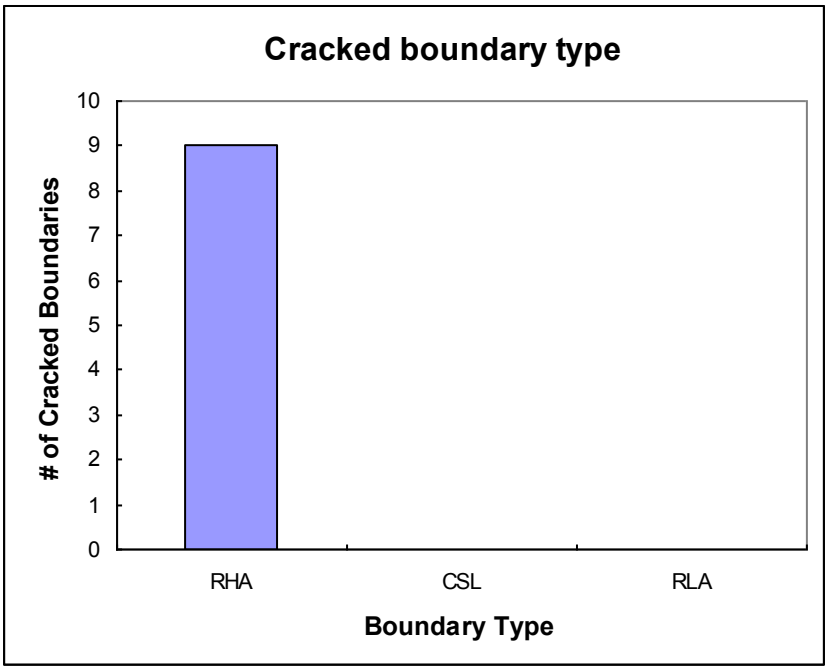

Figure 4.3 Histogram of total number of crack boundaries in regards to boundary type (random high-angle, coincident site-lattice, random low-angle).

Low-angle boundaries typically disappear with increasing deformation, which significantly reduces the possibility of intergranular fracture in this type of boundary. CSL-type boundaries typically emit dislocations easier and at lower resolved stresses, allowing for better GB accommodation compared to RHA boundaries.

4.4.2 Crack angle with respect to tensile direction

Fracture mechanics indicate that cracks propagate easier when there is a high angle between the length of the crack and the tensile direction (highest angle being 90 degrees) [11]. A similar approach could be used for crack initiation at the grain boundary assuming that the free volume present from structural units represents a nano-void. A cluster of structural units could then come together to form a small crack. Figure 4 shows the results for crack angle with respect to the tensile loading direction. This data shows a clear trend of cracking occurring in boundaries where the crack angle is close to perpendicular with the tensile direction. If the

samples were loaded in compression rather than tension, then the current trend would be null since the free volumes would be forced to close rather than open.

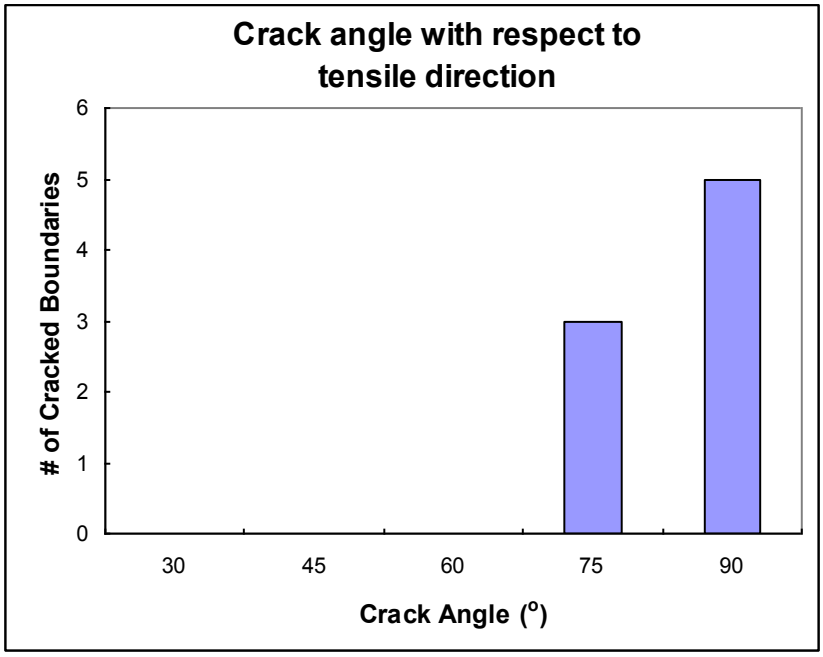

Figure 4.4 Histogram of total number of crack boundaries as a function of the crack angle with respect to the tensile loading direction.

4.4.3 Location of crack formation

Triple junctions are known to stop and store mobile GB dislocations [12]. This process can lead to a build-up of energy and strain, which could possibly affect the generation of a crack. Previous works have noted the formation of nano-cracks due to the effect of the triple junction [12]. We studied the location of crack initiation in our simulated samples to see if the triple junction was or was not causing any effect on the cracked boundaries. This can be seen in Figure 5. It appears that the triple junction does, in fact, play a role in crack generation; however, this may be due to the high volume fraction of triple junctions present in the sample due to the nanocrystalline grain size. The intrinsic limitation on sample size in molecular dynamics simulations restricts us to small grain sizes, which results in much smaller length grain

boundaries. Therefore, the possibility for a crack to form near a triple junction is much higher than in a larger grain sample.

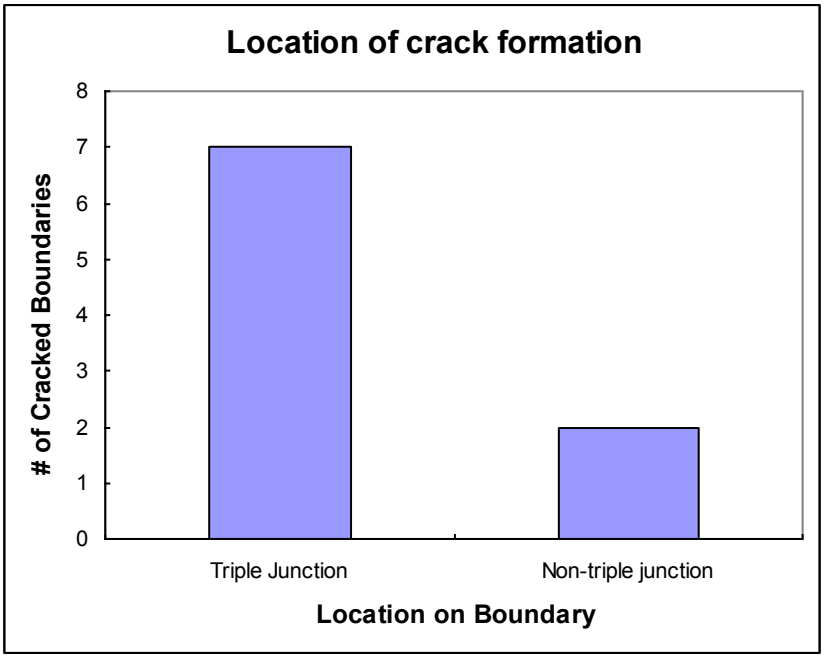

Figure 4.5 Histogram of total number of crack boundaries in regards to location of crack formation along the grain boundary.

4.4.4 Schmid Factor in grains adjacent to cracks

Schmid factors describe how readily a grain is to emit a dislocation based on its preferred slip plane for a given tensile direction. Usually, grains with higher Schmid factors will generate more dislocations because a much lower resolved shear stress is needed to cause the grain to slip and deform. A high Schmid factor could lead to high dislocation activity from a GB, which can reduce the stress build-up or cause large amounts of localized deformation. A low Schmid factor could lead to stress concentration build-up at the GB due to the lack of preferred slip planes for dislocation emission. Figure 6 illustrates the effect of Schmid factor in the grains surrounding the cracked boundary.

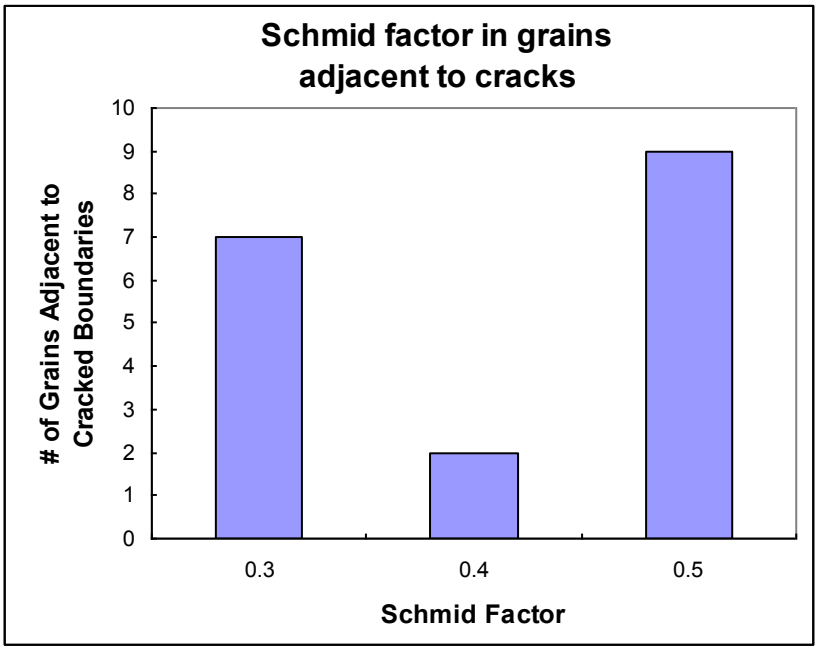

Figure 4.6 Histogram of total number of grains adjacent to cracked boundaries.

No conclusive evidence can be seen for the effect of the Schmid factor in the grains adjacent to the crack. The difference in Schmid factor, however, between the two grains containing the crack may affect the cracking behavior of the GB. This trend is illustrated in Figure 7. All of the cracks formed between grains with a Schmid factor difference less than 0.10.

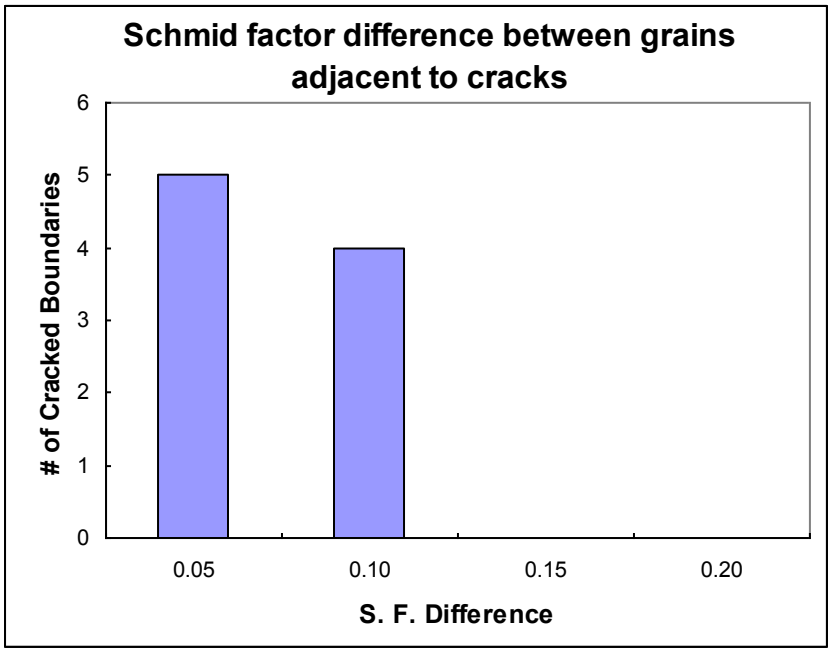

Figure 4.7 Histogram of total number of cracked boundaries as a function of the Schmid factor difference between the two grains containing the crack.

4.4.5 Excess Energy of Cracked Boundary

Thermodynamic properties of boundaries play an important role in capillarity-driven processes such as grain growth, precipitation and coarsening, as well as in solute segregation phenomena and interface decohesion [13]. Although our samples are pure Nickel, the GB energy may still affect the boundaries mobility and corresponding microstructural morphology. The boundary energy has been correlated to free volume in previous works [5, 14, 15], which means a higher energy corresponds to a higher amount of free volume in the interface. This should increase the chance of cracking if treated as a pre-existing crack of clustered structural units. Excess potential energy data was previously collected for the 9g40n sample in Chapter 1 [5]. The boundaries that cracked in this sample all had high energies, greater than 1.43 J/m^2, which was higher than the sample average GB energy of 1.34 J/m^2. This result is somewhat trivial since there is a GB energy dependence on misorientation between the two grains

containing that boundary [5]. Thus, the results are consistent that cracking typically occurs in RHA boundaries, whose excess potential GB energies are often high.

4.4.6 Localized strain of the cracked boundaries

Different grain boundaries and even different regions of the same boundary respond to applied tensile loading differently where the difference in response leads to varying levels of dislocation emission. This results in strain localization that can play a role in crack nucleation [4]. We examined strain localization by generating heterogeneous displacement maps. Heterogeneous displacement is the magnitude of the difference between the adjusted deformed atomic coordinates and the initial position of the atoms[4]. Figures 4, 5, and 6 show the displacement maps for the three samples and their specific cracks at strain intervals preceding the crack formation. The dislocation cores, stacking faults, grain boundaries, and structural units are colored by the black atoms that are filtered by a centrosymmetry parameter [10] greater than 3. The heterogeneous displacements are colored by the range of blue to red where red indicates the largest displacement, therefore, illustrating the strain localization. This is a largely a result of dislocation emission from the boundaries as part of the deformation process, but can also indicate GB sliding in nanocrystalline samples whose average grain sizes are less than 20 nm. A full dislocation is shown by a sharp gradient in the displacement map, which is easily seen in Figure 8.

There is no clear evidence in any of the samples which suggests that strain localization alone is the cause of crack nucleation. The localization of strain appears to be more of an indication that a crack could form. This knowledge coupled with the orientation of the GB in regards to the tensile loading directions serves as the best prediction. For example, GB7-8 and 7-9 in Figure 8 contain significantly more localized strain than GB1-5; however, GB1-5 is the

preferred boundary for intergranular cracking due to its orientation. Also, high dislocation activity at the GB does not always serve as a primary cause for crack nucleation. The cracked boundary in Figure 8 experiences much dislocation emission and absorption, but the cracked boundaries in Figures 9 and 10 experienced little to no dislocation activity.

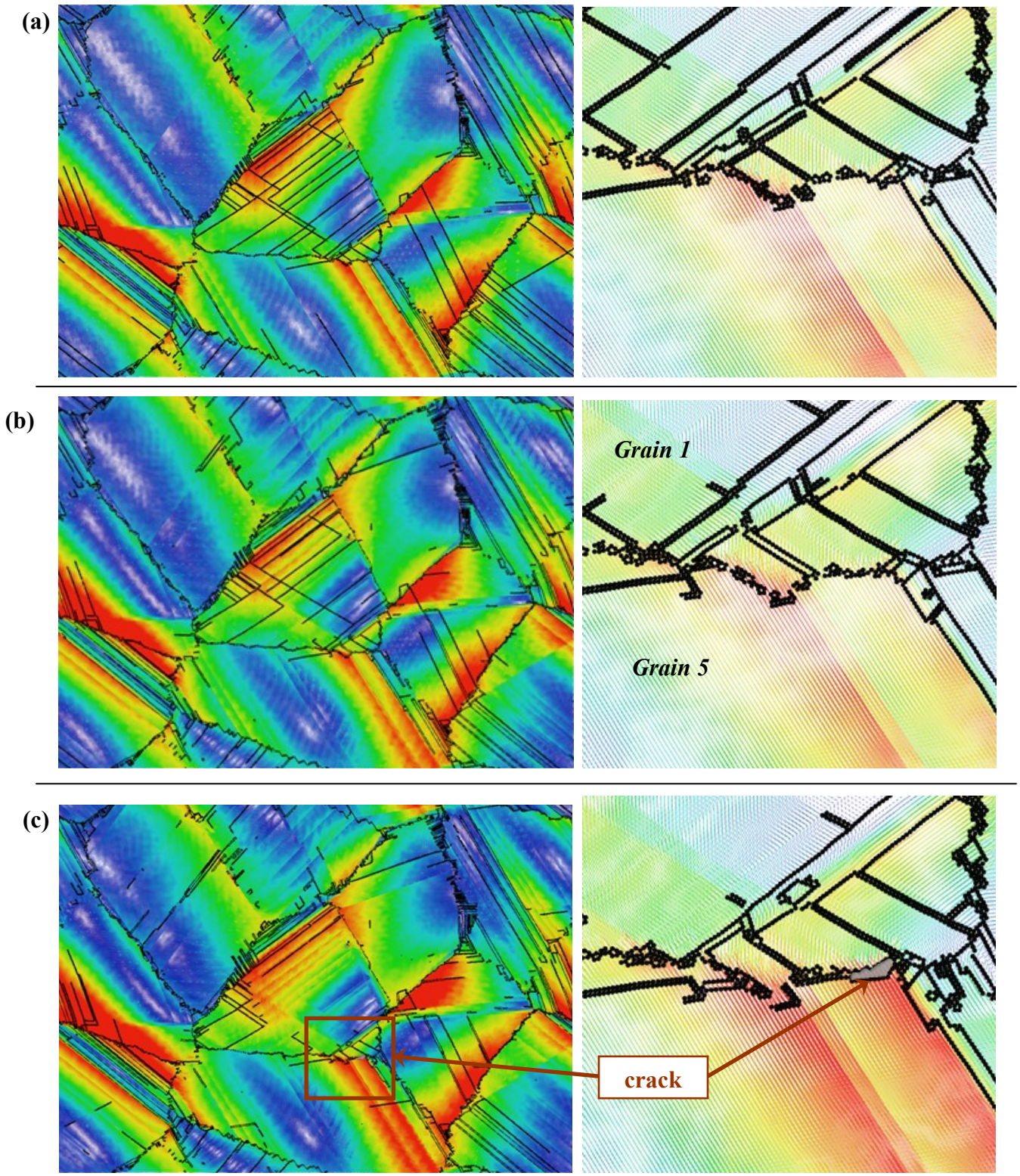

Figure 4.8 Heterogeneous deformation map for GB1-5 in sample 9g40n. Deformation levels of 6, 7, and 8% in the Y-direction are shown. The color map used is from blue to red where red indicates heterogeneous displacements up to 1.1, 1.3, and 1.5 nm. Atoms with centrosymmetry parameter greater than 3 are shown in black.

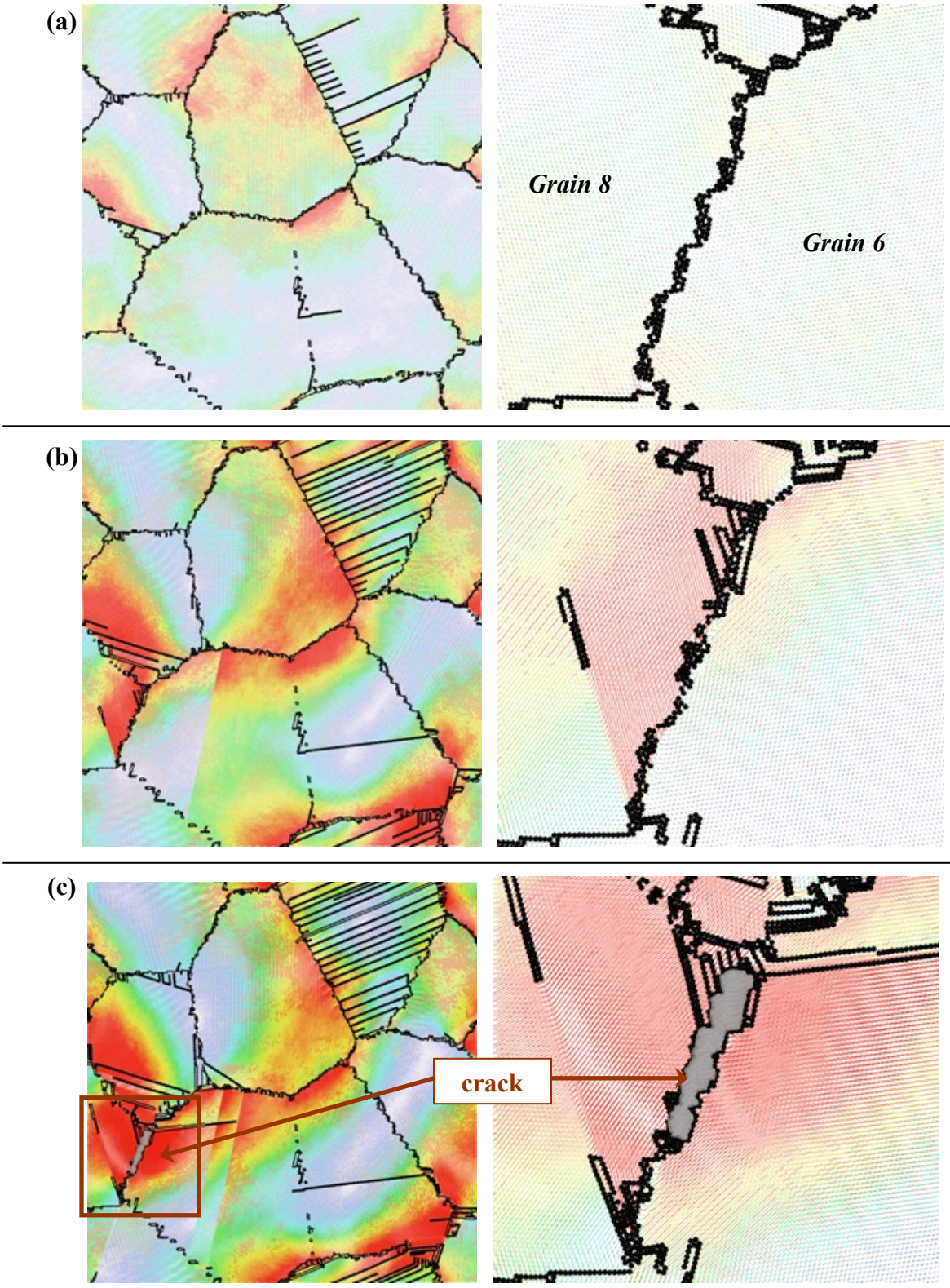

Figure 4.9 Heterogeneous deformation map for GB6-8 in sample TEM2D. Deformation levels of (a) 3, (b) 4, and (c) 5% in the X-direction are shown. The color map used is from blue to red where red indicates heterogeneous displacements up to 0.2, 0.4, and 0.6 nm. Atoms with centrosymmetry parameter greater than 3 are shown in black.

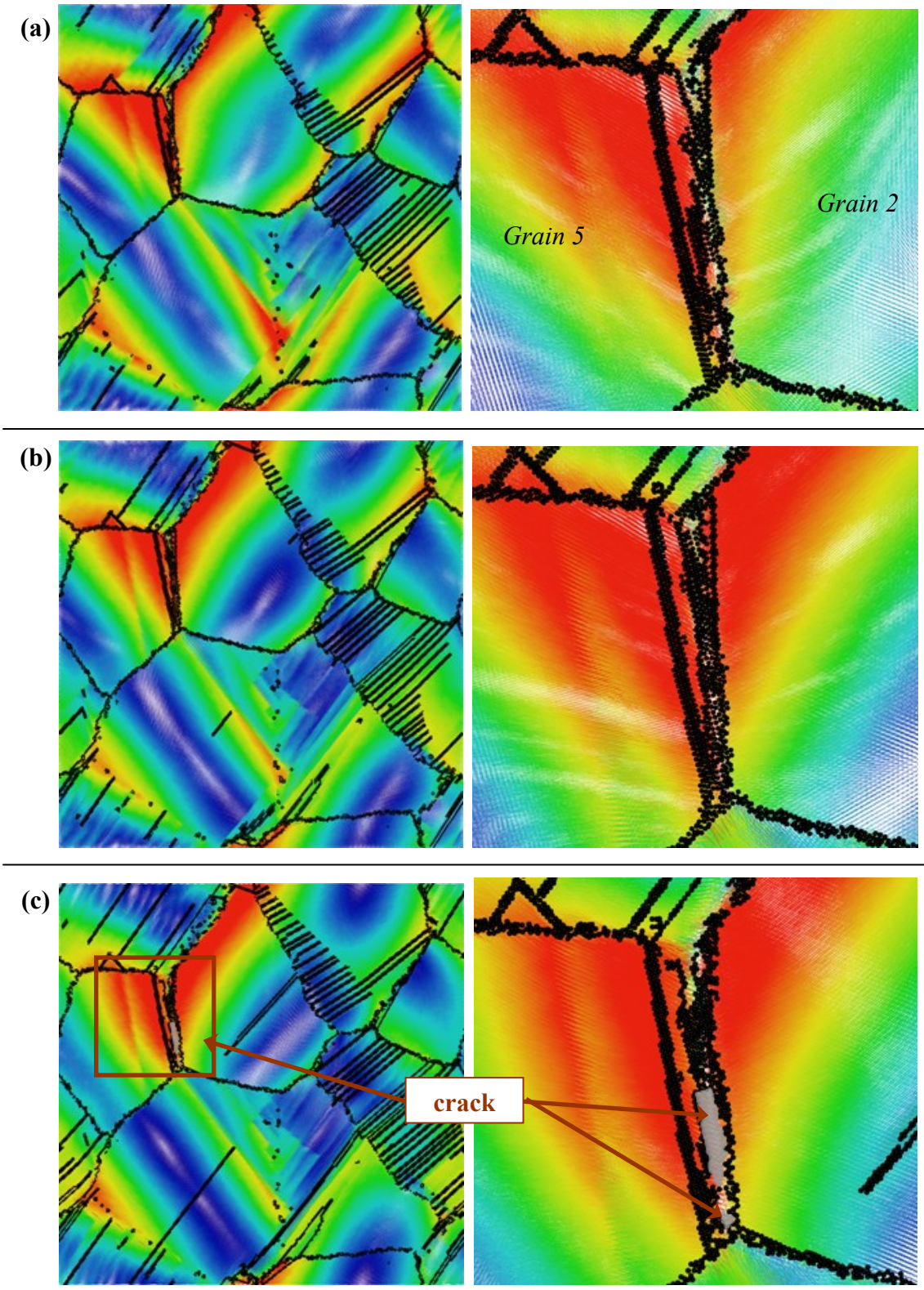

Figure 4.10 Heterogeneous deformation map for GB2-5 in sample TEM3D. Deformation levels of (a) 7, (b) 8, and (c) 9% in the X-direction are shown. The color map used is from blue to red where red indicates heterogeneous displacements up to 0.95, 1.00, and 1.05 nm. Atoms with centrosymmetry parameter greater than 3 are shown in black.

4.4.7 Crack initiation in the modeled TEM sample

A computer generated sample, seen in Figure 2, was made with a thin-film configuration to accurately model an experimental TEM sample, tensely deformed in-situ [6]. The simulated sample had the same grain orientations and grain boundary misorientations as the experimental one, except with two less grains due to the limitations of the Voronoi construction [3] for sample creation, and grain sizes about an order of magnitude smaller due to the time scale limitations of molecular dynamics. The other major difference is the simulated sample is pure Ni, while the experimental sample is 13Cr15Ni austenitic steel; however, both are of the FCC crystal structure.

After running the simulation to 15% strain in the X-direction, the model sample was found to crack in GB2-5. This is a RHA boundary that has a high crack angle (80.7^{o}) with respect to tensile direction, and has Schmid factors of 0.47 and 0.49 in the two surrounding grains. The experimental sample, however, cracked at GB's 2-8 and 3-8. These are both RHA boundaries with a medium crack angle (47^{o}) with respect to tensile direction, and have Schmid factors of 0.47 and 0.38 in the three surrounding grains. A picture of the crack comparison in the experimental and model sample can be seen in Figure 11. A more detailed picture of the crack and dislocation activity in the model sample is shown in Figure 10c. The crack did not form in the same grain boundary meaning that the simulated sample did not exactly model the behavior of the experimental sample. This is most likely due to the lack of making grains with exactly the same shape and size as well as GB's with the same GB orientation in regards to the tensile direction. Also, there is variance because the experimental sample is an alloy with precipitates that has been irradiated while the model sample is defect-free, pure Ni. Nevertheless, it is still important to note that the cracks were consistent in RHA type boundaries between grains with high Schmid factors.

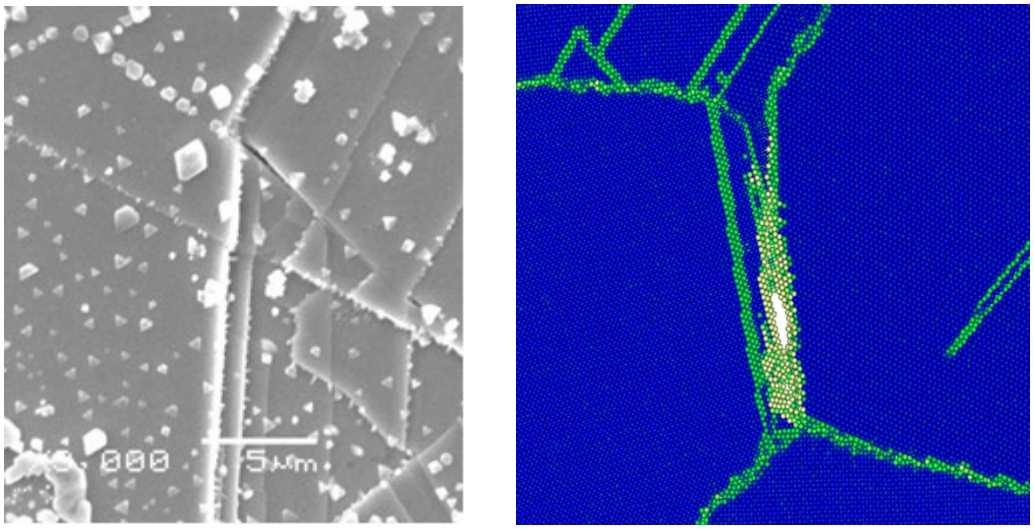

Figure 4.11 Comparison of crack nucleation in the (a) experimental sample [6] used under fair use guidelines and (b) model sample with thin-film configuration. The color map used in (b) is the centrosymmetry parameter ranging from 0 (blue) to 12 (yellow).

4.5 Conclusions

Three samples were tested in regards to both x- and y- tensile deformation for a total of nine cracked grain boundaries to study the trends in intergranular cracking behavior. All of the cracks analyzed were found to occur in RHA boundaries whose crack angle was large (> 64^{o}) with respect to the tensile loading direction. The majority of the cracks (> 75%) occurred near a triple junction suggesting a possible added effect of decreased ductility near that portion of the GB. The magnitude of the Schmid factor in grains adjacent to the cracked boundary did not appear to have any affect on crack nucleation; however, the Schmid factor difference was small (< .10) between all grains containing a cracked boundary. The excess potential GB energy was consistent in being high for the boundaries that formed cracks, which corresponds to the misorientation of that GB, specifically noting the RHA boundaries. There was no apparent effect of strain localization near a GB on crack nucleation, but the map of localized strain could be used

in conjunction with boundary orientation to serve as a prediction. The results from this simulation study are very consistent with those perform on experimental samples of various austenitic steels [2]. The only difference in intergranular cracking behavior comes from the magnitude of the Schmid factors in grains adjacent to the cracked boundaries where [2] reports high Schmid factors in grains containing cracked boundaries. Also, the experimental results do not contain any studies on the effects of grain boundary energy or strain localization.

A computer generated sample of pure Ni was modeled after an experimental sample of 13Cr15Ni austenitic steel in hopes of accurately reproducing the cracking behavior. The model sample cracked in a different boundary than the experimental sample, but did occur in a RHA boundary between grains of high Schmid factors. Further work is needed in creating simulated samples that have exactly the same grain shape and GB orientation as experimental samples.

4.6 References

1. Cao, A.J. and Y.G. Wei, *Atomistic simulations of crack nucleation and intergranular fracture in bulk nanocrystalline nickel.* Physical Review B, 2007. **76**(2): p. 5.
2. McMurtrey, M., G. Jiao, and G. Was, *Crack Analysis of Irradiated Austenitic Steel.* via Private Communication, 2009.
3. Farkas, D. and W.A. Curtin, *Plastic deformation mechanisms in nanocrystalline columnar grain structures.* Materials Science and Engineering a-Structural Materials Properties Microstructure and Processing, 2005. **412**(1-2): p. 316-322.
4. Farkas, D. and L. Patrick, *Tensile deformation of fcc Ni as described by an EAM potential.* Philosophical Magazine, 2009. **89**(34-36): p. 3435-3450.
5. Floyd, N.P., *Chapter 2: Energetics and Plastic Deformation Behavior of <110> Random Tilt Grain Boundaries.* Thesis, 2010.
6. *13Cr15Ni Austenitic Steel Grain Clusters for Use in Strain Modeling.* via Private Communication, 2009. Fair Use determination attached.
7. Floyd, N.P., *Chapter 3: Plastic Deformation of Thin-flim with Random Grain Boundary Structure.* Thesis, 2010.
8. Plimpton, S., *Fast Parallel Algorithms for Short-Range Molecular Dynamics.* Journal of Computational Physics, 1995. **117**(1): p. 1-19.
9. Mishin, Y., et al., *Interatomic potentials for monoatomic metals from experimental data and ab initio calculations.* Physical Review B, 1999. **59**(5): p. 3393-3407.
10. Kelchner, C.L., S.J. Plimpton, and J.C. Hamilton, *Dislocation nucleation and defect structure during surface indentation.* Physical Review B, 1998. **58**(17): p. 11085-11088.

11. Dowling, N.E., *Mechanical Behavior of Materials*. 3rd ed. 2007, Upper Saddle River: Pearson.
12. Gutkin, M.Y., I.A. Ovid'ko, and N.V. Skiba, *Emission of partial dislocations from triple junctions of grain boundaries in nanocrystalline materials.* Journal of Physics D-Applied Physics, 2005. **38**(21): p. 3921-3925.
13. Mishin, Y., M. Asta, and J. Li, *Atomistic modeling of interfaces and their impact on microstructure and properties.* Acta Materialia, 2010. **58**(4): p. 1117-1151.
14. Wolf, D., *Structure-energy correlation for grain-boundaries in fcc metals - 3. Symmetrical tilt boundaries* Acta Metallurgica Et Materialia, 1990. **38**(5): p. 781-790.
15. Spearot, D.E., *Evolution of the E structural unit during uniaxial and constrained tensile deformation.* Mechanics Research Communications, 2008. **35**(1-2): p. 81-88.

Chapter 5: Effect of Deformation Temperature on Deformation Behavior of Random Grain Boundaries

5.1 Abstract

Molecular dynamics simulations are used to study the effect of deformation temperature on plastic deformation behavior and the interactions between dislocations and grain boundaries in model FCC polycrystalline samples. The two samples include a sudo-2D sample with columnar grains and a thin-film sample with 3D grain orientations. Heterogeneous displacement maps were made for a side-by-side comparison of deformation temperature to qualitatively assess the dislocation activity and the various interactions with the grain boundaries. Furthermore, the results from the simulated samples are compared with preliminary results of experimentally deformed austenitic steel samples.

5.2 Introduction

Deformation of metallic materials occurs largely through dislocation emission and movement as well as interactions between the dislocations and grain boundaries. Grain boundaries themselves can aid in the deformation process via the generation of dislocations or even slow the deformation process via the hindering of dislocation transfer across the boundary. At high temperature, the atoms in a material become excited leading to complex interactions, especially as more than one slip system becomes activated by the grain boundary. Many materials, such as those used to convert thermal energy to electrical energy, are used in high temperature environments requiring the need to understand how they perform under load.

This paper focuses on the effect of high temperature versus room temperature deformation behavior and its effect on the interaction of grain boundaries with dislocations in a

virtual FCC polycrystalline sample of Ni. Two samples are utilized, one with columnar grains and the other as a thin-film, to represent two possibilities of computer simulated samples for comparison with experimental samples [1] made of various austenitic steels. The deformation simulations are ran at 300K and 700K using molecular dynamics to model the atomic interactions via the embedded atom method.

5.3 Methodology

Two digital samples with the same grain layout, but different grain configuration, were created to study the effects of temperature on deformation behavior. The first sample, labeled TEM2D, has a grain and grain boundary network that was generated using a Voronoi construction [2] with specified grain orientation and boundaries similar to an experimental TEM sample, but only using two Euler's angles (ϕ_1 and ϕ_2). This sudo-2D sample, as shown in Figure 1, has columnar grains tilted around <110> and periodic boundary conditions in all three dimensions, so that there are no surface effects. The second sample, labeled TEM3D, was generated using a Voronoi construction with all three Euler's angles specified to obtain a fully 3D oriented sample that was 3nm thick with free surfaces in the z-direction and periodic boundary conditions in the other two. This thin-film sample, as also shown in Figure 1, has the same X-Y grain layout as the TEM2D sample, but instead has the addition of inclined grains and grain boundaries. The grain boundaries in both samples were relaxed via a high temperature treatment by heating to 700K and cooling back to 300K in 100ps. These are the same TEM2D and TEM3D samples used from the cracking behavior study in Chapter 4 [3] seen in Figure 1.

The program used for the molecular dynamics simulation is LAMMPS [4] using a Nose-Hoover thermostat and barostat to control the temperature and pressure with a well known interatomic potential of Mishin et at for Ni [5]. Both samples were tensely deformed in the X-

direction at a rate of 3.3×10^{8} s^{-1} up to 15% strain at two different temperatures, 300 and 700K. For the TEM2D sample, the pressure was kept at zero in directions perpendicular to the tensile axis to preserve the periodic boundary conditions. For the TEM3D sample, the pressure was also allowed to vary in the Z-direction due to its free surface. For deforming the samples at 700K, the sample temperature was first increased from 300K to 700K over 30ps, and then the deformation simulation was run starting at 0% strain. Data for individual atoms was recorded every 1% strain including atomic position, centrosymmetry, and stress in order to study the deformation behavior and create pictures for comparison at low and high temperature.

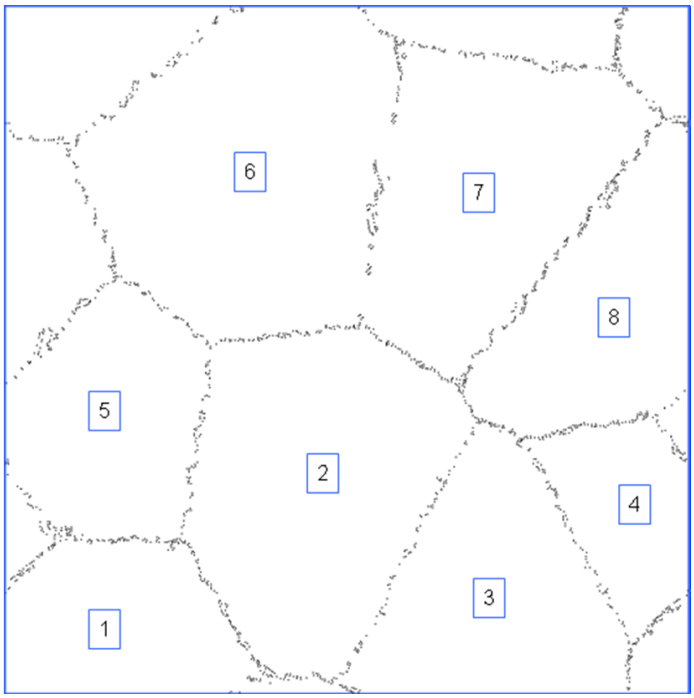

Figure 5.1 TEM2D and TEM3D sample layout in the (110) projection with 8 grains, approx. 20 nm in diameter, relaxed by heating to 1200K and cooling back to 300K in 100ps.

5.4 Results and Discussion

5.4.1 Temperature dependence on deformation response in a sample with columnar grains

The columnar grain sample, labeled TEM2D, was tensely deformed in the X-direction at both 300K and 700K to compare the effect of temperature on the same initial sample. At plastic deformation up to approximately 3% strain, the sample appears to behave similar between the two deformation temperatures, beyond which the two deviate significantly. In order to examine full dislocations and complete deformation behavior at each strain level, heterogeneous displacement maps were created by normalizing the deformed atomic coordinates to their original positions. Figure 2 shows a side-by-side comparison of the displacement maps at 3, 4, and 5% for the sample at 300 and 700K. Sharp gradients in the color of the maps indicate a complete dislocation that has passed through the grain and resulted in slip. A broad look at the sample reveals a significantly more amount of dislocation activity at 700K as well as additional slip systems becoming active.

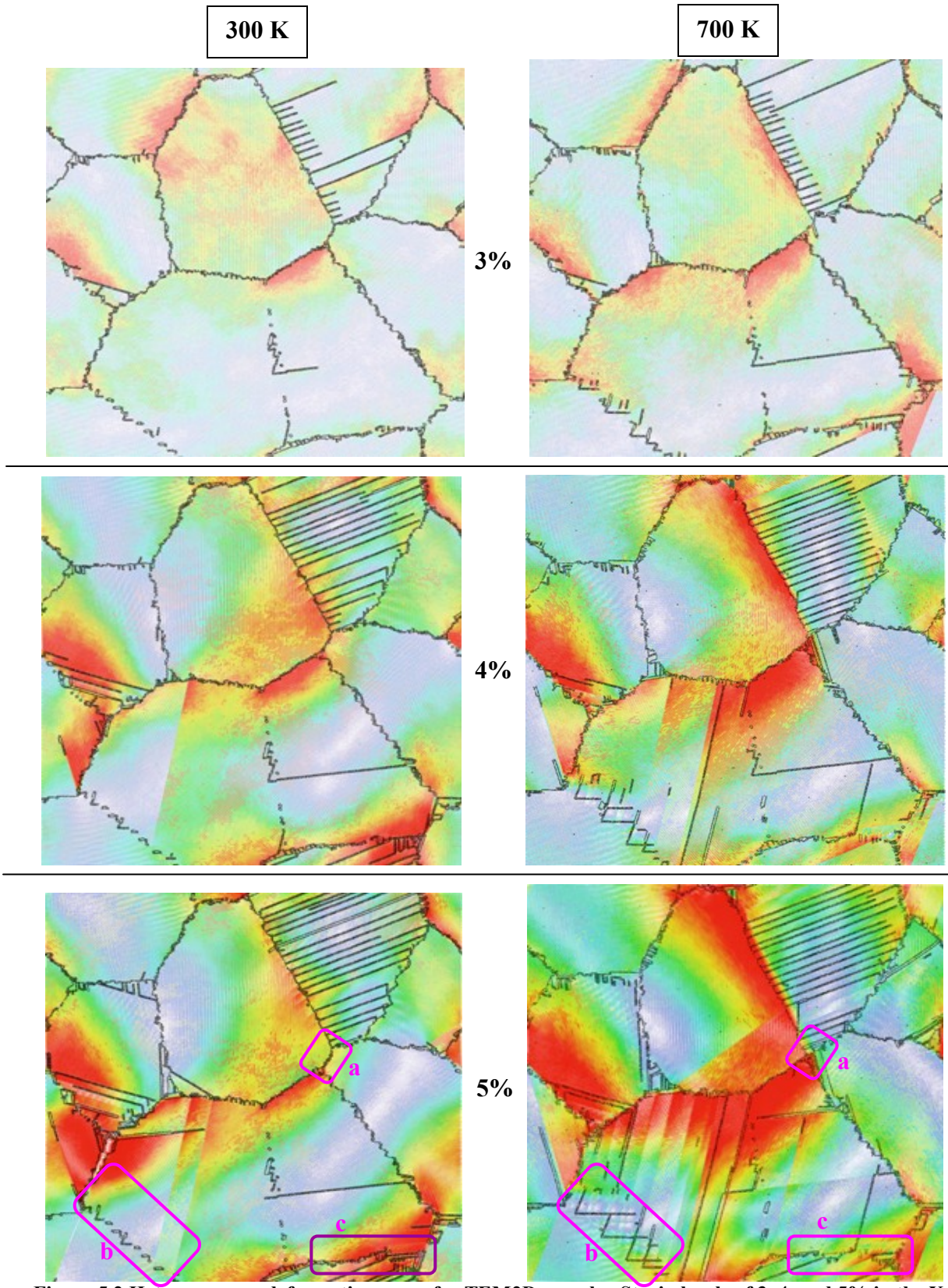

Figure 5.2 Heterogeneous deformation maps for TEM2D sample. Strain levels of 3, 4, and 5% in the X-direction are shown. The color map used is from blue to red where red indicates heterogeneous displacements up to 0.25, 0.55, and 0.8 nm. Atoms with centrosymmetry parameter greater than 3 are in black. Areas of interest outlined in pink.

Boundary areas in the sample with extreme differences between the two temperatures were labeled and outlined in pink. The first area of interest, labeled *a*, details the small interface of GB2-8 with grain 3 directly above. The GB gets consumed and disappears at 700K, while remaining unaffected at 300K. This is due to the movement of GB2-3, shown in Figure 3, as a result of grain boundary diffusion at high temperature.

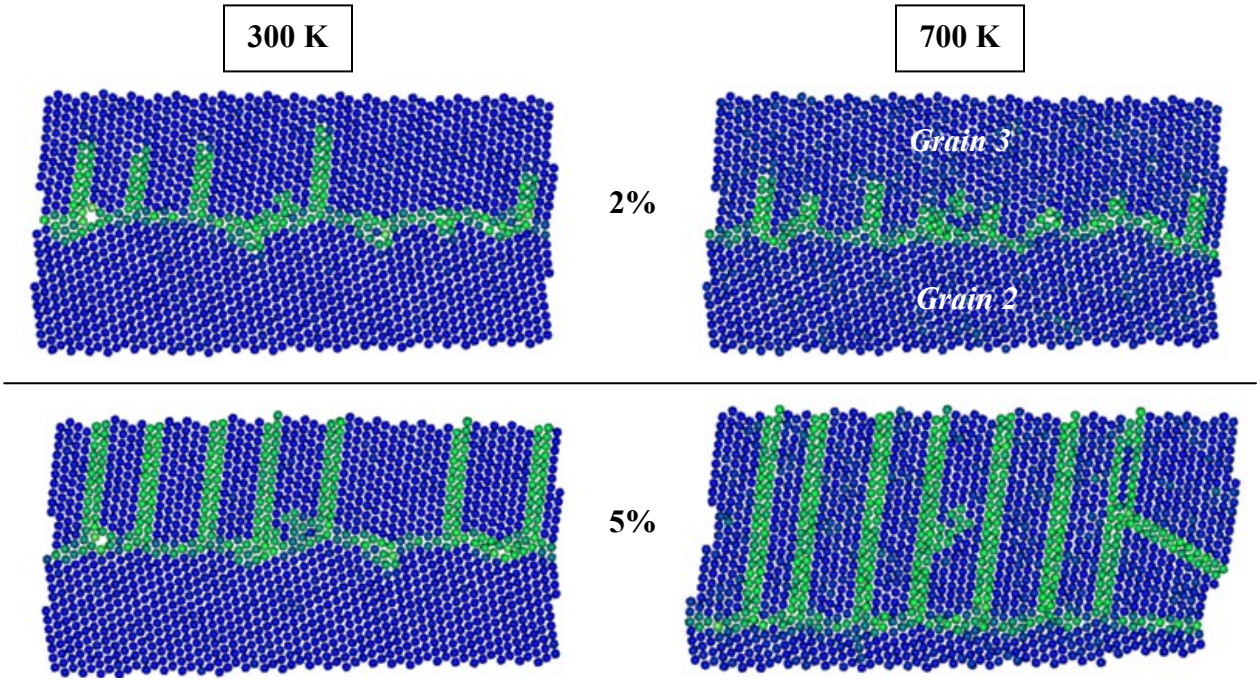

Figure 5.3 Detail of GB2-3 in TEM2D sample at 2% and 5% strain illustrating movement of the GB perpendicular to the GB plane. Atoms colored with the centrosymmetry parameter from 0 (blue) to 12 (yellow).

Another area of interest in Figure 2 is *b*, which outlines a low-angle boundary between grains 1 and 6. At 300K, the boundary consists of small dislocation debris segments where only a couple of dislocations are emitted. At 700K, GB1-6 emits many dislocations resulting in slip bands shown in grain 6 at 5% strain. The boundary structure here is constituted by an array of extended stacking faults indicating that the GB wants to move, likely due to the increased temperature. A closer look at the outlined area *c* in Figure 2 can be seen in Figure 4, a RHA boundary with a misorientation angle of 16.9^{o}. The sample at 700K emits a full dislocation from

GB3-7 across the bottom corner of grain 7 into the adjacent boundary at 4% strain. This most likely changes the lattice misorientation in that small region into a close to low-angle boundary allowing slip through that GB. The 700K sample achieves this though more active slip systems since the higher temperature reduces the critical resolved shear stress needed to emit a dislocation. This is also confirmed by the emission of a partial dislocation followed by a stacking fault shown vertically into grain 7 at 700K where this does not occur at 300K.

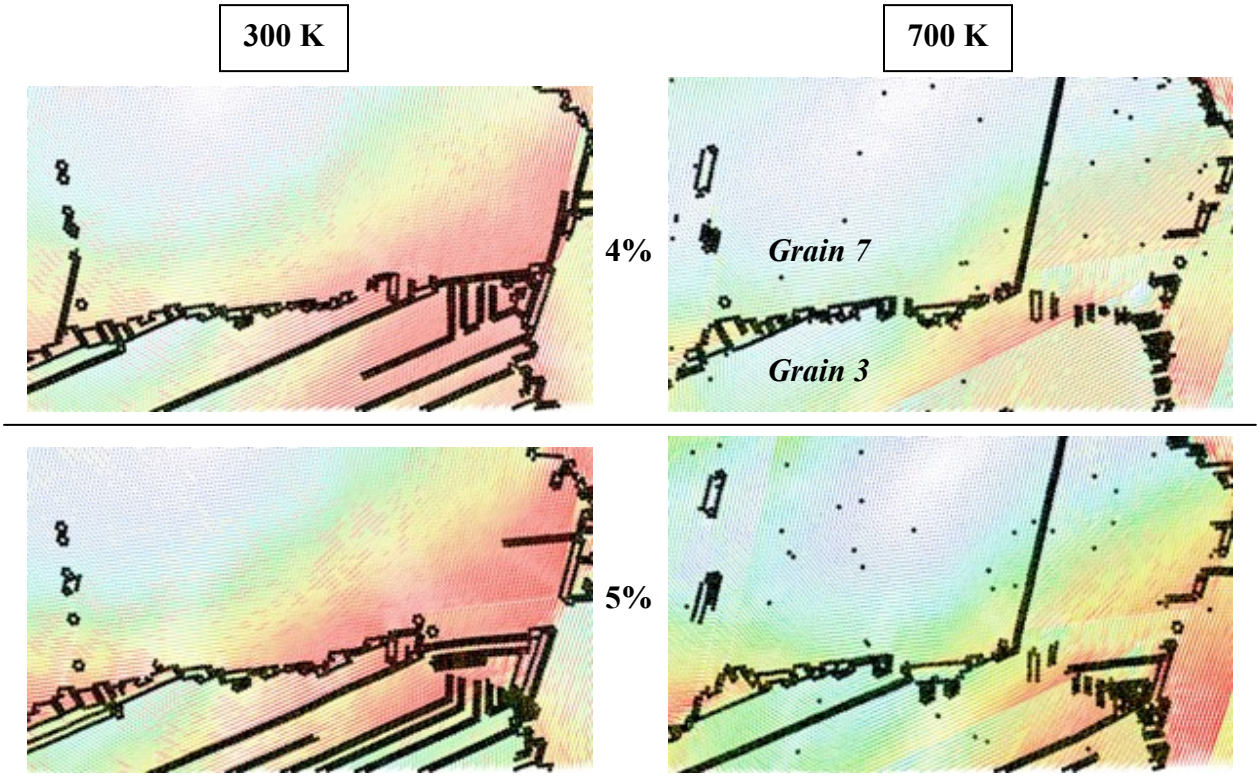

Figure 5.4 Detail of GB3-7 for TEM2D sample at 4% and 5% strain, denoted by pink box "c" in Fig. 5.2, utilizing the same heterogeneous displacement color map.

In addition to local differences, the deformation temperature also played a significant role in the overall mechanical behavior response of the sample. This is illustrated by the stress-strain curve as shown in Figure 5. The large differences in deformation behavior occur from 3% strain and beyond, which corresponds to the findings from the heterogeneous displacement maps. When deformed at 300K, the sample experiences a period of hardening followed by crack

formation at 5% strain. The sample deformed at 700K was much softer due to its increased dislocation activity and did not form any cracks through the entire deformation simulation. The sample at 700K also experienced small amounts of GB sliding, which was an additional deformation mechanism. Figure 6 shows a representation of the typical GB sliding behavior between the two deformation temperatures. The increased thermal energy at 700K aided the atom movements that resulted in sliding. It is important to note that GB sliding was not observed in all the boundaries at 700K, and the amount of sliding seen at 300K was considering insignificant.

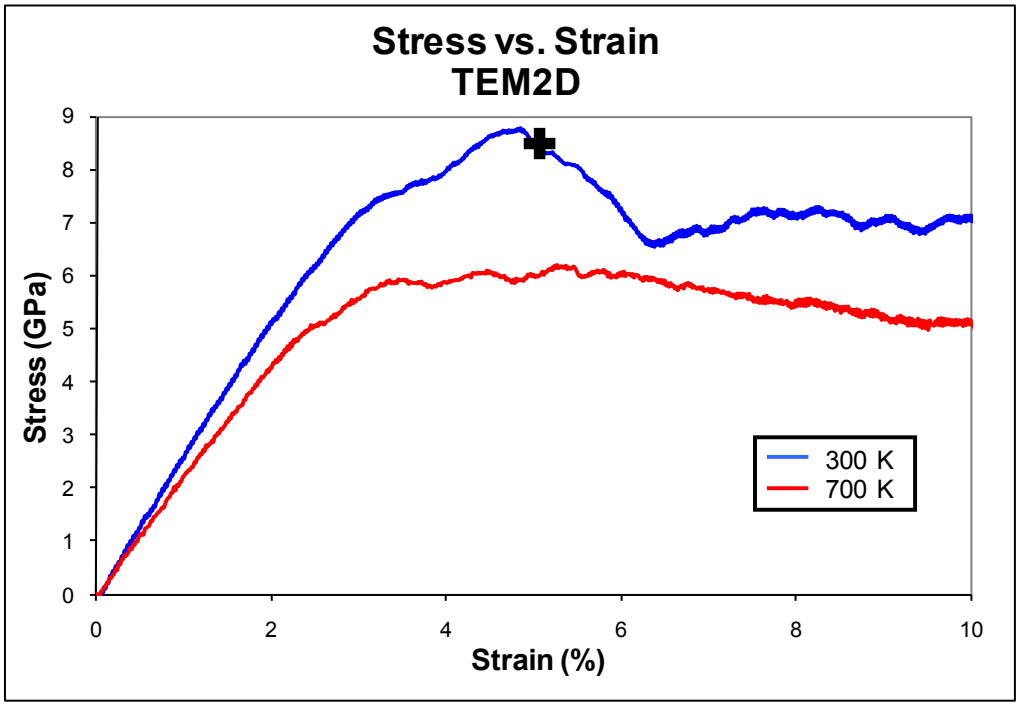

Figure 5.5 Stress-Strain curves for the columnar grain sample tensely deformed at 300 and 700 K. The black "+" indicates the point of crack formation. No cracks formed in the 700K deformed sample.

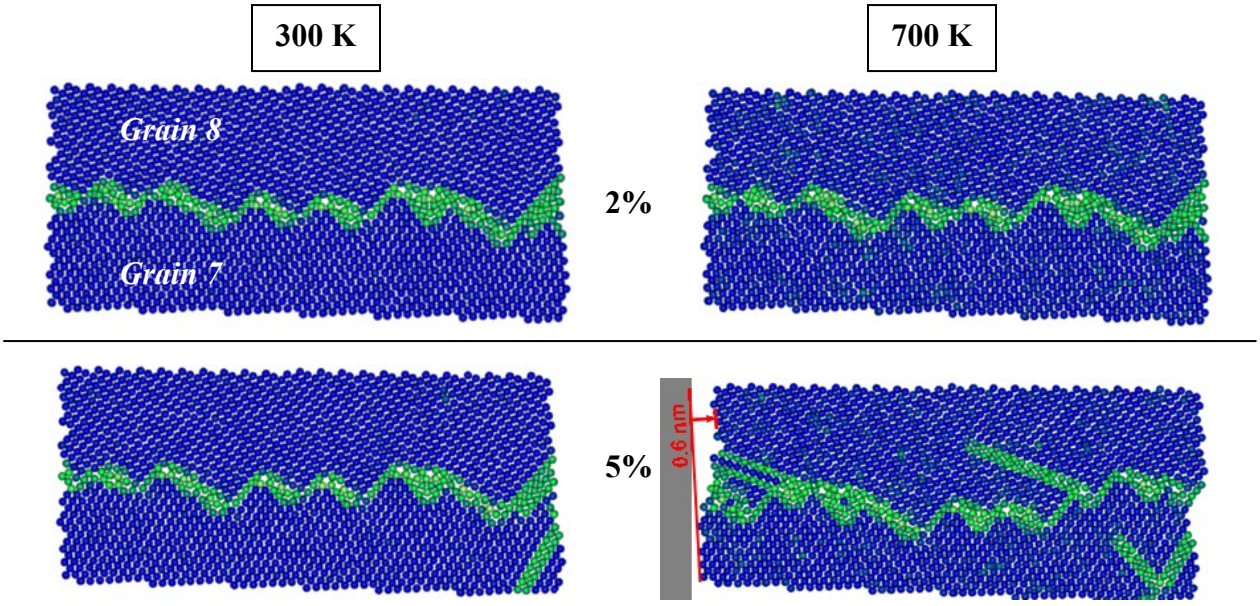

Figure 5.6 Detail of GB7-8 in TEM2D sample at 2% and 5% strain illustrating grain boundary sliding. Atoms colored with the centrosymmetry parameter from 0 (blue) to 12 (yellow). The amount of sliding, in nm, is calculated in red for the sample at 700K.

5.4.2 Temperature dependence on deformation response in a thin-film sample

Similar to the previous sample, the thin-film sample, labeled TEM3D, was tensely deformed in the X-direction at both 300K and 700K. This sample, however, had a defined thickness and free surfaces in the Z-direction in order to give a 3-dimensional representation of the grains and GB planes. For plastic deformation up to approximately 3% strain, the sample at the two deformation temperatures behaved alike, beyond which the two deviated considerably. Again, heterogeneous displacement maps were generated for a side-by-side comparison of the dislocation activity and complete deformation behavior, which is displayed in Figure 7. For all visual analyses, a 6Å thick slice was made through the center of the sample perpendicular to the Z-axis to remove any noise from the top and bottom surfaces. A broad look between the two deformation temperatures reveals a slightly more amount of dislocation emission in the 700K sample, but more importantly, farther/faster dislocation travel at 700K for the same corresponding strain levels. Also, two extra slip systems are observed to become active at 700K than at 300K.

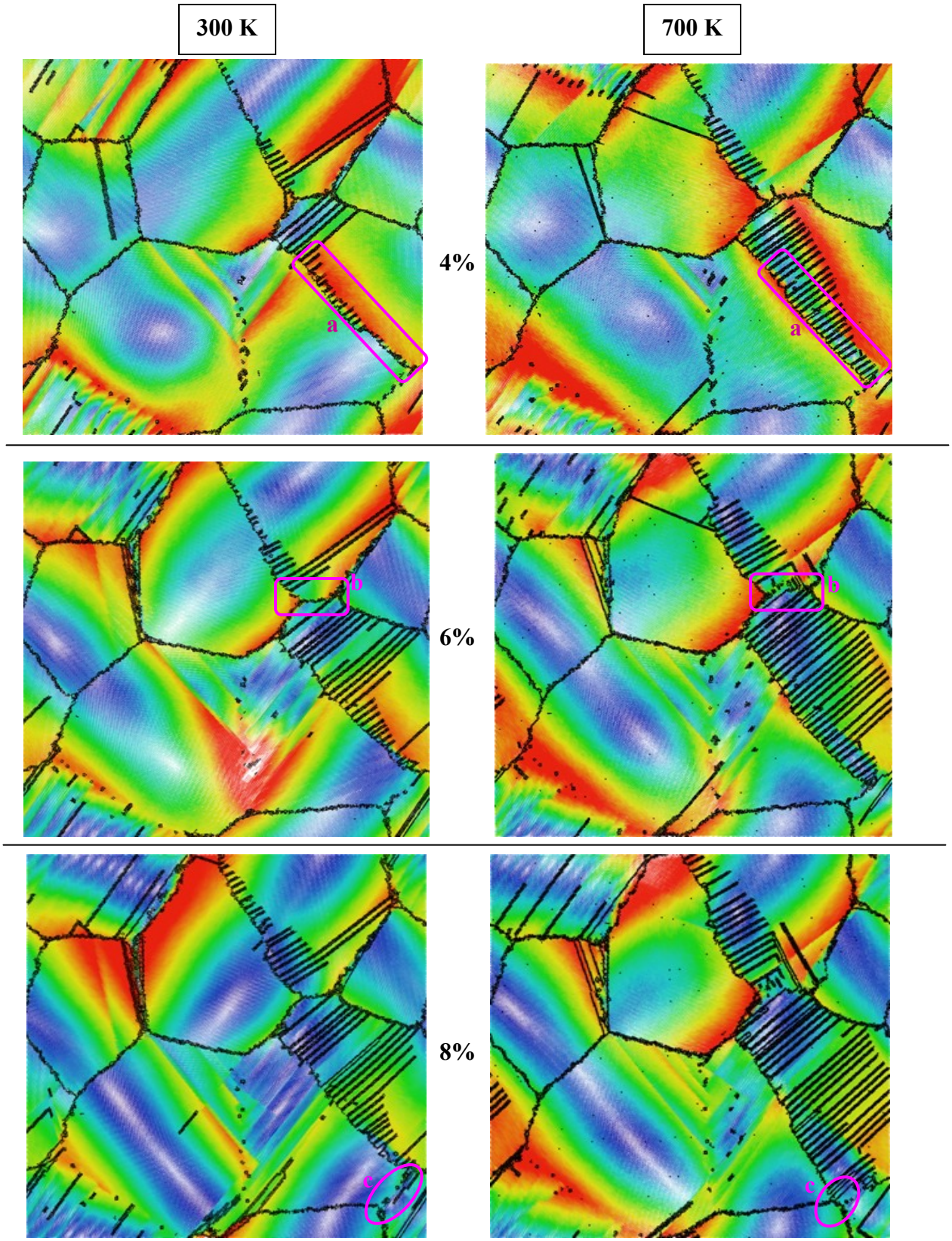

Figure 5.7 Heterogeneous deformation maps for TEM3D sample shown at strain levels of 4, 6, and 8% in the X-direction. The color map used is from blue to red where red indicates heterogeneous displacements up to 0.5, 0.75, and 0.95 nm. Atoms with centrosymmetry parameter greater than 3 are in black. Areas of interest outlined in pink.

For a more detailed analysis, different regions of the sample at the two different temperatures are labeled and outlined in pink in Figure 7. The first area of interest is labeled *a*, which is a Σ3 boundary made of grains 7 and 8. A close-up can be seen in Figure 8. Significantly more dislocations are emitted earlier from this GB at 700K and travel faster across the grain due to the elevated temperature that caused a decrease in the critical resolved shear stress. As this emission process proceeds at high temperature, GB 7-8 moves considerably from its original position, which then consumes GB 1-7. This details the second area of interest, labeled c, where GB1-7 remains about the same for the sample deformed at 300K. Once again, the elevated temperature assists in GB diffusion allowing for easier movement and conformations.

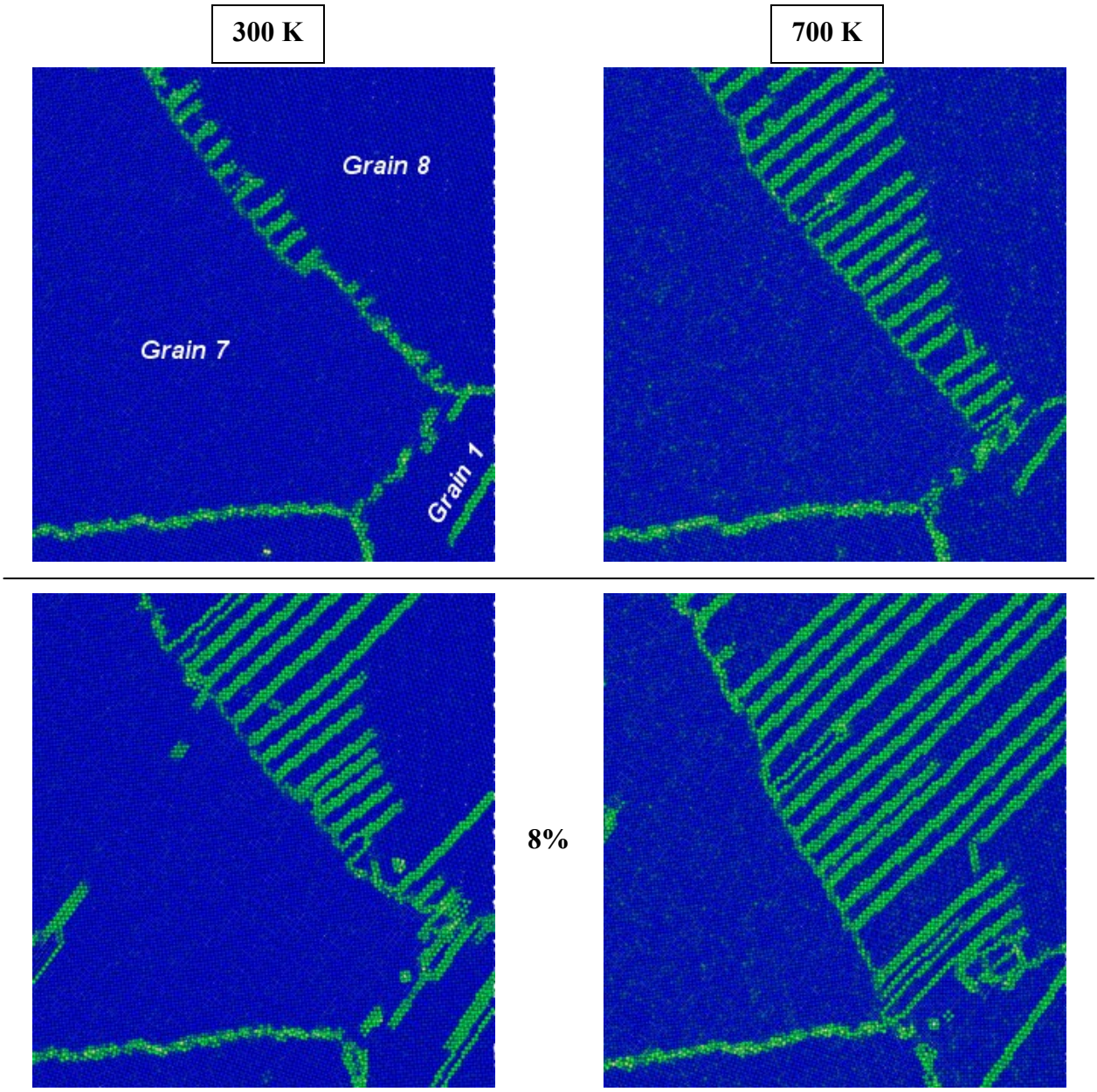

Figure 5.8 Detail of GB7-8 and 1-7 in TEM3D sample at 4% and 8%, denoted by pink boxes *a* and *c* in Fig. 5.7. Atoms colored with the centrosymmetry parameter from 0 (blue) to 12 (yellow) to illustrate boundary movement perpendicular to GB plane.

The other particularly interesting area, denoted by the pink box *b* from Fig. 7, is detailed in Figure 9. A large difference in the behavior of this RHA boundary can be seen between the two deformation temperatures. At 700K, GB3-8 sees a twinning dislocation that begins to transform the interface into a low-angle boundary. The elevated temperature allows a second slip system to become active in grain 3 which helps emit dislocations from GB3-8 and further

assist the twinning dislocation to glide across grain 8. This behavior is not seen in the sample at 300K since the additional slip system does not become active.

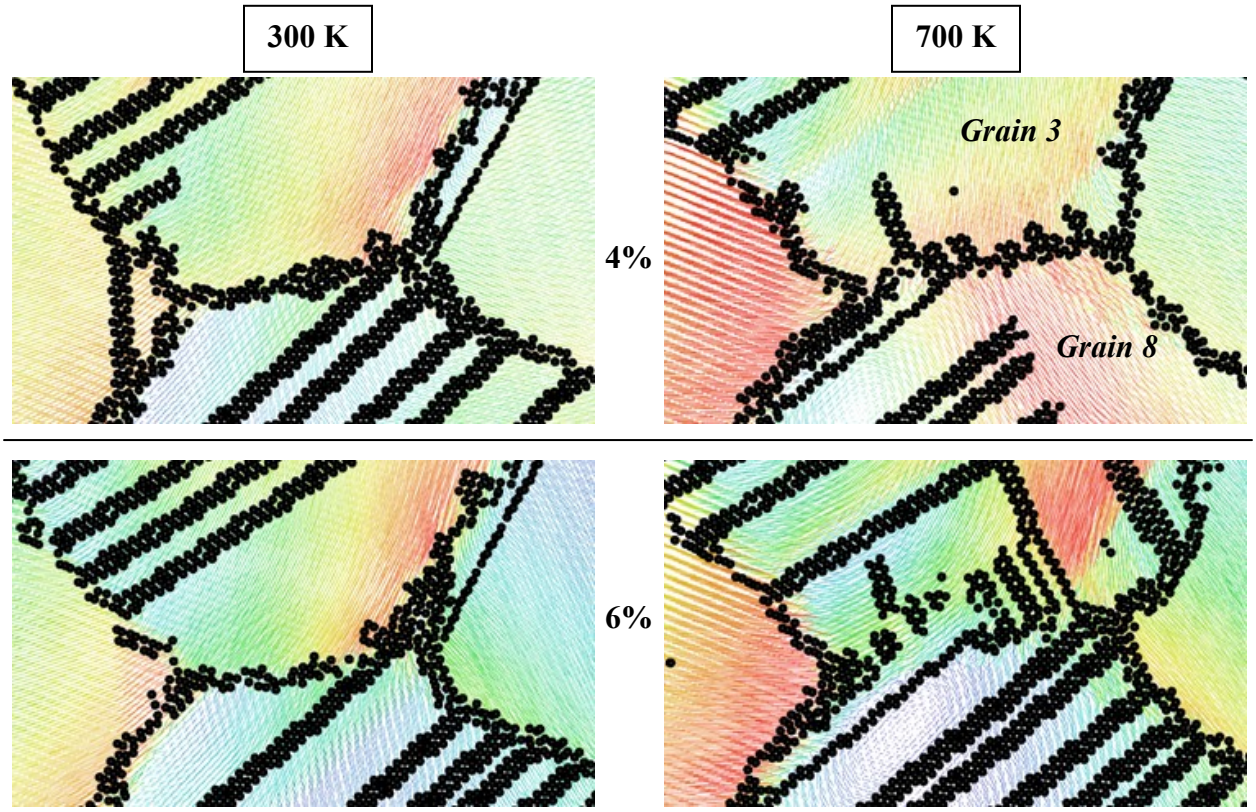

Figure 5.9 Detail of GB3-8 for TEM3D sample at 4% and 6% strain, denoted by pink box *b* in Fig. 5.7, utilizing the same heterogeneous displacement color map.

The overall mechanical behavior response can be seen by the stress-strain curve given in Figure 10. The two curves follow similar behavior up to about 3%, but then the sample deformed at 700K continues to follow a trend of softer behavior at about 0.5 -1 GPa lower than 300K throughout the remainder of the deformation period. Also, cracking occurs later at 700K around 11% strain compared to 8% strain at 300K. These differences are simply a result of the heightened temperature allowing more deformation in the sample at 700K. In addition to dislocation deformation, both samples experienced a similar degree of GB sliding. Figure 11 illustrates the typical sliding behavior seen in the sample. For this particular boundary, the

extent of sliding was about 0.3nm at both deformation temperatures. It is important to note that no sliding or at least limited sliding should had been observed for the 300K deformed sample since it went through a high temperature relaxation treatment [6]; however, the sample at both deformation temperatures experienced GB sliding in approximately 1/5 of all the boundaries. This is likely a result of the thin-film configuration due to the limited thickness of the sample. When compared with the columnar grain sample, the thin-film sample exhibited strengths about 2.5 times lower over the course of plastic deformation. The decrease in strength comes from the increase in possible slip systems in the thin-film sample due its 3D grain configuration as well as a significant additional amount of GB sliding.

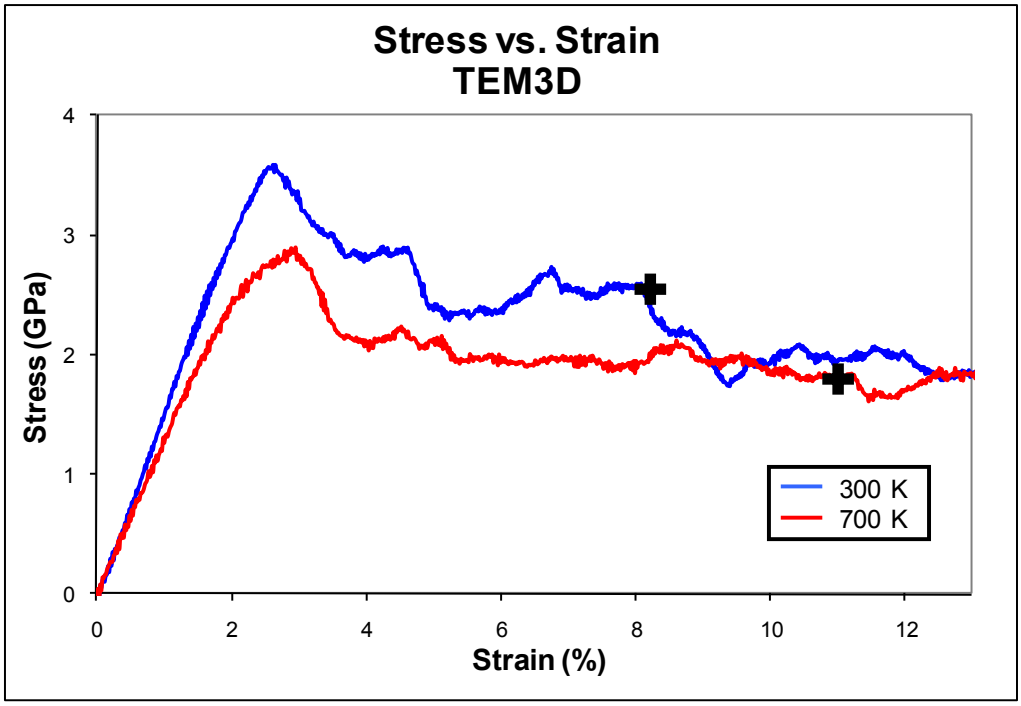

Figure 5.10 Stress-Strain curves for the thin-film sample tensely deformed at 300 and 700 K. The black "+" indicates the point of crack formation.

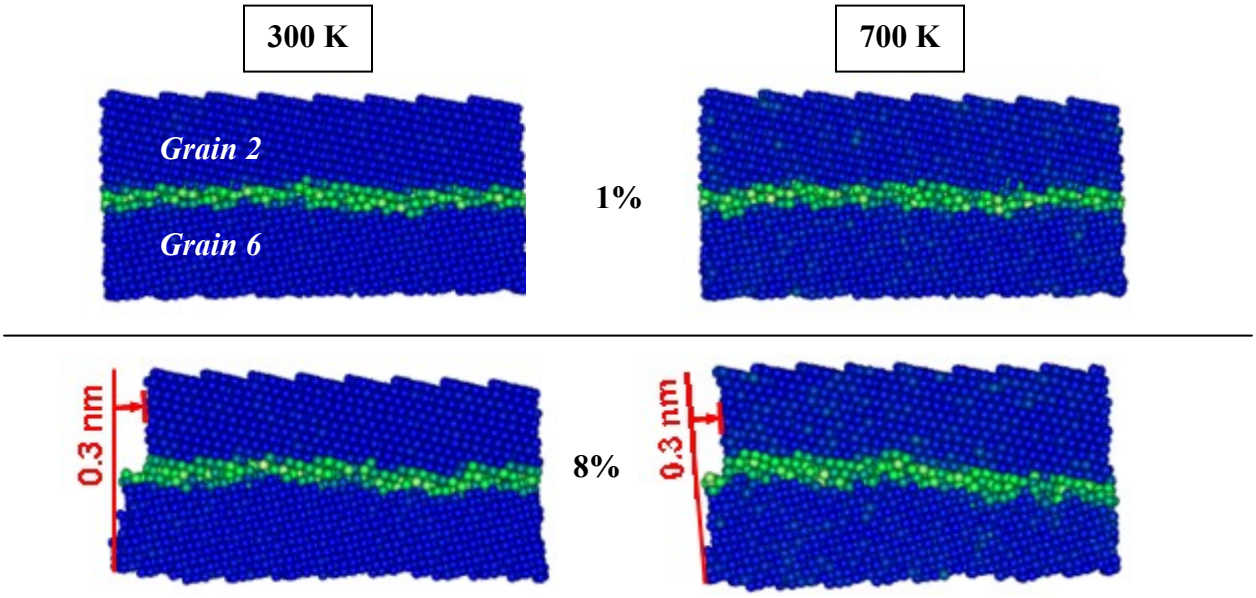

Figure 5.11 Detail of GB2-6 in TEM3D sample at 1% and 8% strain illustrating grain boundary sliding. Atoms colored with the centrosymmetry parameter from 0 (blue) to 12 (yellow). The amount of sliding, in nm, is calculated in red.

5.4.3 Dislocation transfer across the boundary

Another important aspect about dislocation behavior, in addition to emission activity and travel speed across a grain, is the transfer of dislocations across the grain boundary. Grain boundaries act as a block to dislocations moving from one grain to another until a critical shear stress is met to cause transfer. Dislocation transfer will lead to additional deformation in an adjacent grain and allow slipping of the boundary. In both samples studied, dislocation transfer was only observed in the TEM2D sample at 700K across a Σ3 as shown in Figure 12. At 3% strain, the red arrow shows the path of the partial dislocation through grain 3 before it arrives at the boundary. At 4% strain, the partial dislocation displaces a small portion of GB3-4 and leaves behind a stacking fault. The blue arrow shows the displacement of the boundary as a result of the incoming partial. At 5% strain, another partial dislocation follows along the same path and fixes the stacking fault, which then transfers across the boundary into grain 4. This results in the passing of a full dislocation across GB3-4 through both grains as indicated by the dotted red line.

The dislocation transfer mechanism occurs at 700K and not 300K because the heightened temperature decreases the critical shear stress needed allow transfer.

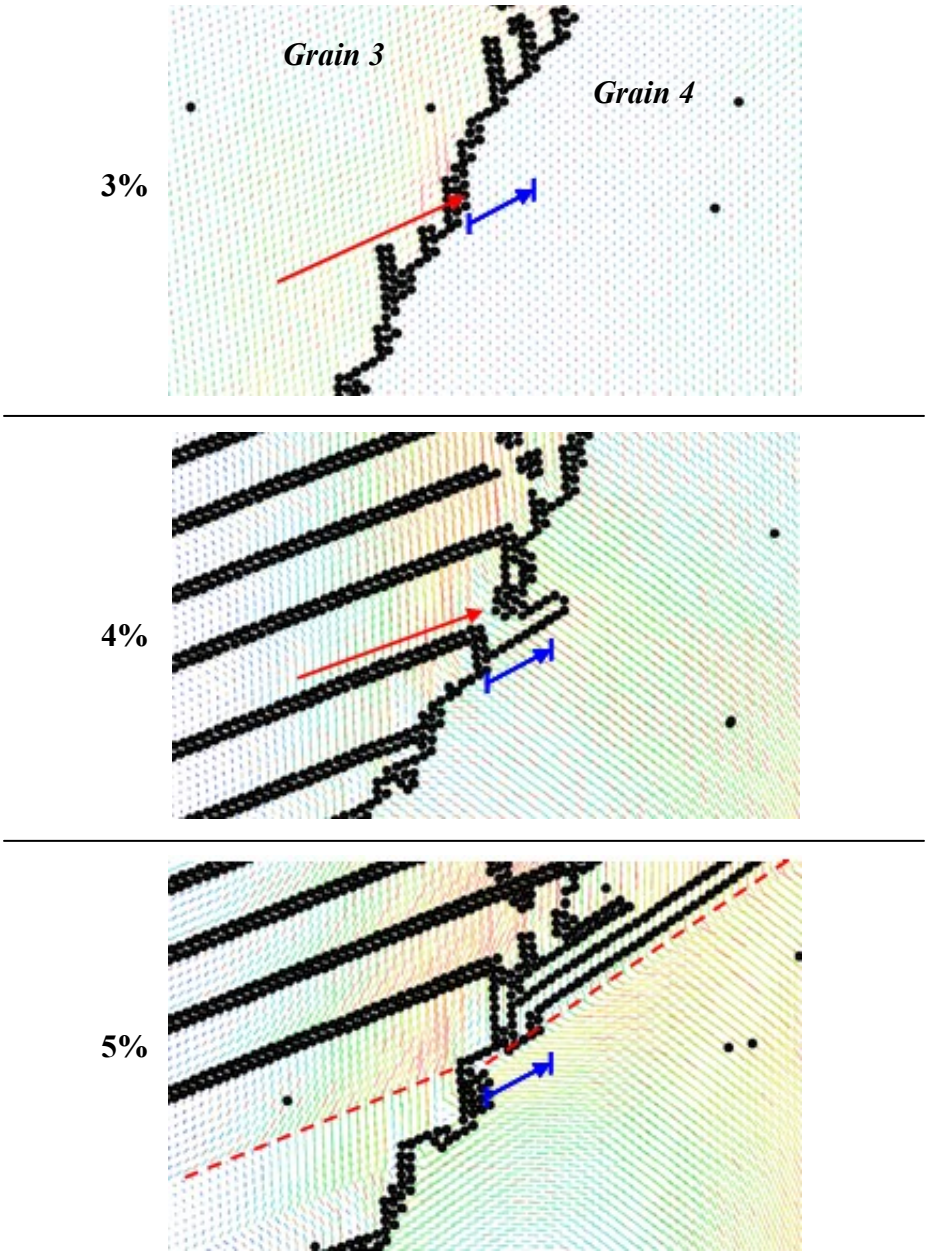

Figure 5.12 Detail of GB3-4 in TEM2D sample at 3, 4, and 5% strain deformed at 700K. Dislocation transfer shown across the Σ3 boundary. The color map used is from blue to red where red indicates heterogeneous displacements up to 0.25, 0.55, and 0.8 nm. Atoms with centrosymmetry parameter greater than 3 are in black. Red arrows represent movement of partial dislocation, blue arrow serves are a reference for boundary displacement, and red dotted line is the result of a full dislocation, a.k.a. slip.

5.4.4 Comparison with experimental samples

In-situ deformation experiments have been performed on irradiated TEM specimens of various austenitic steels at low and high temperatures under the coordination of the University of Illinois and the University of Michigan. Through private communication, preliminary results have been obtained for comparison with computer-modeled samples to see the effect of temperature on dislocation interactions with a grain boundary [7]. The experimental samples were deformed at 300 and 673K compared to the simulated samples deformed at 300 and 700K.

They note that the dislocation transfer mechanism across a grain boundary at high temperature seems to be faster than those observed at room temperature, and in general, there is a greater propensity for grain boundary slip at high temperature. The dislocation transfer mechanism across a coherent twin boundary at 400^{o}C is detailed in Figure 13. First, multiple partial dislocations are emitted on a single plane into the adjacent grain and then perfect dislocations follow while continuing to be emitted on a single plane. Eventually, transfer ceases into this adjacent grain and dislocations are emitted into the incoming grain. These results are comparable with the transfer mechanism shown in Figure 12 for a coherent $\Sigma 3$ such that a partial is first emitted followed by a complete dislocation. Also, transfer is only observed at high temperature for the computer-modeled samples similar with the increased transfer activity for experimental samples at high temperature.

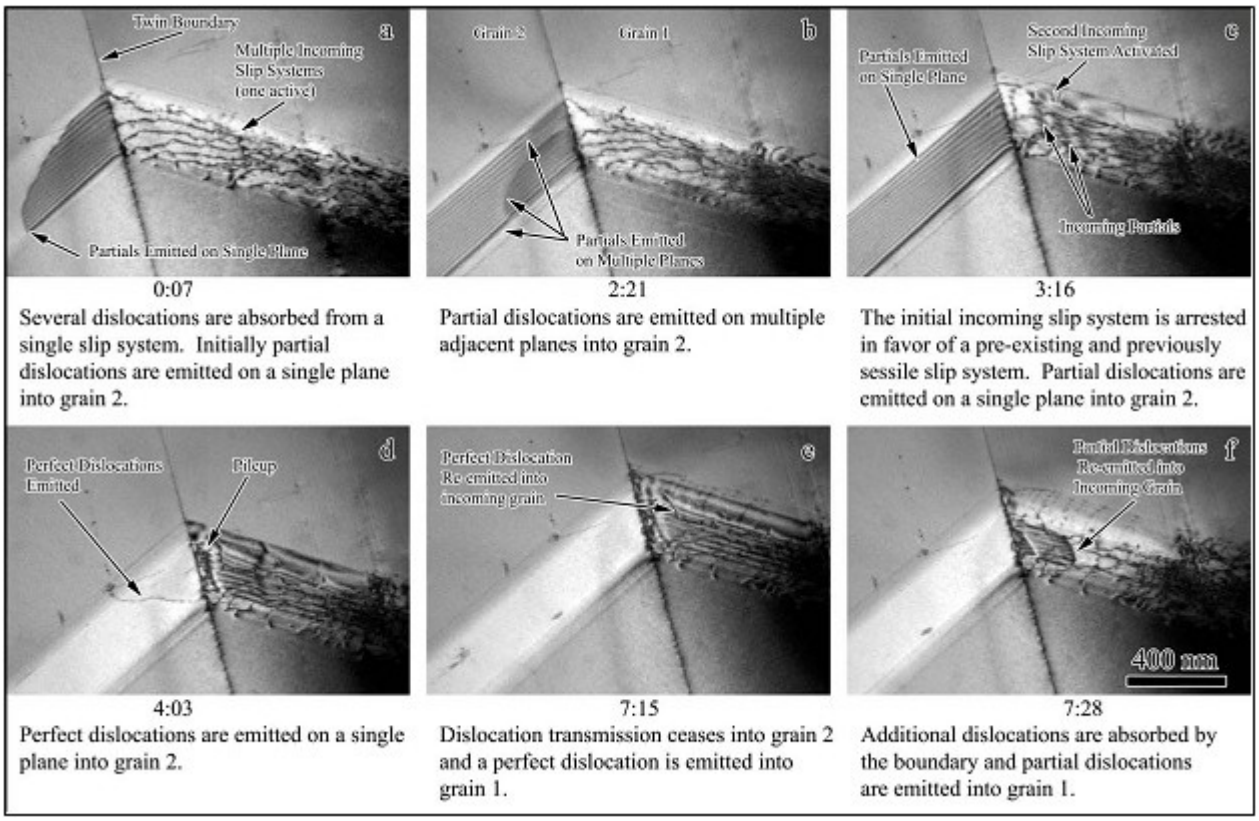

Figure 5.13 Experimental sample made of 304SS showing the dislocation transfer mechanism across a coherent twin boundary at 400°C [7] used under fair use guidelines.

5.5 Conclusions

Two computer-generated samples of Ni were created, one with columnar grains (TEM2D) and the other with a thin-film configuration (TEM3D), and deformed at 300 and 700K to study the effects of temperature on deformation behavior. For both samples, an increased amount of dislocation emission and faster travel was observed, which lead to more deformation as indicated in the corresponding stress-strain curves. The elevated temperature at 700K increased the amount of active slip systems allowing even more dislocation generation. Also, the onset of cracking was delayed in both samples deformed at 700K. Significant grain boundary movement occurred in at least one GB for both samples at 700K and not at 300K, showing an

increased affect of dislocation accommodation by the grain boundaries at high temperature. Most importantly, dislocation transfer across a Σ3 was observed at 700K confirming similar results performed on experimental samples of austenitic steels.

5.6 References

1. *13Cr15Ni Austenitic Steel Grain Clusters for Use in Strain Modeling.* via Private Communication, 2009.
2. Farkas, D. and W.A. Curtin, *Plastic deformation mechanisms in nanocrystalline columnar grain structures.* Materials Science and Engineering a-Structural Materials Properties Microstructure and Processing, 2005. **412**(1-2): p. 316-322.
3. Floyd, N.P., *Chapter 4: Cracking Behavior of Random Grain Boundaries.* Thesis, 2010.
4. Plimpton, S., *Fast Parallel Algorithms for Short-Range Molecular Dynamics.* Journal of Computational Physics, 1995. **117**(1): p. 1-19.
5. Mishin, Y., et al., *Interatomic potentials for monoatomic metals from experimental data and ab initio calculations.* Physical Review B, 1999. **59**(5): p. 3393-3407.
6. Vo, N.Q., et al., *Limits of hardness at the nanoscale: Molecular dynamics simulations.* Physical Review B, 2008. **78**(24).
7. *Localized Deformation and Intergranular Fracture of Irradiated Alloys Under Extreme Environmental Conditions.* via Private Communication, 2009. Fair Use determination attached.

Chapter 6: Conclusions and Recommendations for Future Research

6.1 Thesis conclusions

Computer generated samples of pure Nickel with GB-type distributions similar to real samples were created, plastically deformed, and examined as a baseline understanding to the underlying mechanisms of deformation and intergranular fracture in FCC metals used inside of nuclear reactor chambers, specifically austenitic steels. First, a columnar grain sample with all <110> random tilt grain boundaries was utilized to analyze the excess potential energies of the boundaries as a function of grain misorientation, temperature, and plastic deformation and then further correlate those energies to structure evolution during deformation. Deformation in this sudo-2D sample occurred mostly through the emission of dislocations from the random tilt boundaries and was similar to the process that occurs in symmetrical tilt boundaries. This process changed the local boundary structure by collapsing the structural units and shifting nearby atoms, which resulted in changes in the excess potential boundary energy accompanied by changes in the boundary free volume.

Next, a thin-film sample with a 3D grain configuration and free surfaces in the Z-direction was utilized to more accurately model an experimental sample. Plastic deformation was found to be consistent with that of the columnar grain sample in regards to dislocation emission dependence on local grain boundary structure and Schmid factor. Due to the limited thickness of the thin-film, significant grain boundary sliding was observed to occur, which contributed to the deformation process. This would not occur in a larger grain, bulk metal. High temperature deformation simulations were then performed to study the effects of temperature on the deformation behavior as would be for real materials used in-service. An increased amount of

dislocation emission and faster travel was observed at high temperature. The elevated thermal energy of the atoms increased the amount of active slip systems, which allowed even more dislocation generation. Also, the onset of cracking was delayed in both samples deformed at 700K. Most importantly, dislocation transfer across a Σ3 was observed at 700K confirming similar results performed on experimental samples of austenitic steels.

In order to study the source of intergranular fracture, three digital samples, including the ones used for examining the deformation mechanisms, were tested in both the X- and Y-direction and resulted in a total of 9 cracks. All of the cracks were found to occur in RHA boundaries whose crack angle was large with respect to the tensile loading direction. The majority of the cracks occurred near a triple junction suggesting an added effect of decreased ductility near that portion of the GB. The Schmid factor difference was small (< .10) between all grains containing a cracked boundary. The cracking results from this simulation study are very consistent with those performed on experimental samples of various austenitic steels. The only difference in intergranular cracking behavior comes from the magnitude of the Schmid factors in grains adjacent to the cracked boundaries where experiments observe high Schmid factors in grains containing cracked boundaries. To determine how accurate the simulation was in modeling the cracking behavior of a real material, the created thin-film sample was modeled directly after an experimental sample of 13Cr15Ni austenitic steel. It cracked in a different boundary than the experimental one, but was still consistent with the general cracking trends.

6.2 Future work

While the deformation behavior and cracking trends of simulated pure Ni agree well with current experimental samples of austenitic steels, more work is necessary to more accurately model the real metal behavior, specifically in regards to the exact grain boundary which forms

the initial crack. This will eventually involve introducing defects such as vacancies and additional metals to the system, but the current simulation technique needs to be further optimized. The 3D grain configuration of the thin-film sample is vital for modeling the experimental samples; however, a thicker sample (up to 3x) is necessary for removing the free surface effects and eliminating the mechanism of GB sliding. Also, more computer-generated samples need to be created and simulated to make a more conclusive conclusion to intergranular crack initiation.

Aside from sample creation, a quantitative analysis of the number of dislocations needs to be developed instead of the current quantitative method via the heterogeneous displacement maps. This analysis would also help detect dislocation channels and pile-ups, which are difficult to visualize with the current method. Also, a free volume calculation needs to be utilized instead of the coordination number, since the coordination number only approximates the relative free volume present. This can be used to further analyze the correlation between energy, structure, and deformation in future works.

Appendix

A1. LAMMPS Instruction Code Examples

```
# High temperature equilibration (700 K) using Ni Mishin Potential
#TEM3D Digital Sample (w/ free surfaces)

units       metal
boundary    p p s

atom_style  atomic
read_data       NiTEM2thickfs.atoms
mass            1 58.69
#replicate 1 1 2
pair_style  eam/alloy
pair_coeff  * *  niyuri.pot   Ni

neighbor        2.0 bin
neigh_modify      delay 10

compute     new  all  temp

velocity    all  create 300.0 5812775 temp new
compute       centro  all centro/atom
compute       pea  all pe/atom
compute       stress  all stress/atom

dump            1 all custom  5000 dump.htequil id  x y z  c_centro c_pea
#dump_modify     1 scale no
thermo            500
thermo_modify   lost warn  norm yes  temp new
#fix               1 all nve
fix              1 all npt 300.0 700.0 0.25 aniso  0.0 0.0  0.0 0.0  NULL
NULL  0.1 drag 0.1
fix              2 all temp/rescale 10 300.0 700.0 10.0 1.0
fix_modify  2 temp new
timestep    0.001
run         50000
unfix 1
unfix 2

fix              1 all npt 700.0 300.0 0.25 aniso  0.0 0.0  0.0 0.0  NULL
NULL  0.1 drag 0.1
fix              2 all temp/rescale 10 700.0 300.0 10.0 1.0
fix_modify  2 temp new
timestep    0.001
run         50000
```

```
# Metal tensile test simulation (X-Tens Deformation to 15% strain)
# Low temperature (300 K) deformation using Ni Mishin Potential
# TEM2D Digital Sample

units       metal
boundary    p p p

atom_style  atomic
read_data       Ni_tem1.atoms
mass            1 58.69
#replicate 1 1 2
pair_style  eam/alloy
pair_coeff  * *  niyuri.pot   Ni

neighbor        2.0 bin
neigh_modify      delay 10

compute     new  all  temp

velocity    all  create 300.0 5812775 temp new
compute       centro  all centro/atom
compute       pea  all pe/atom
compute       stress  all stress/atom

dump            1 all custom  30000 dump.tensile id  x y z  c_centro c_pea
c_stress[2] c_stress[4]
#dump_modify     1 scale no
thermo            500
thermo_modify   lost warn  norm yes  temp new
#fix              1 all nve
fix              1 all npt 300.0 300.0 0.25 aniso  NULL NULL  0.0 0.0  0.0
0.0  0.1 drag 0.1
fix              2 all temp/rescale 10 300.0 300.0 10.0 1.0
fix              3 all deform 1000 x final -401.97 401.97  units box
fix_modify  2 temp new
timestep    0.001
run         450000
```

```
# Metal tensile test simulation (X-Tens Deformation to 15% strain)
# High temperature (700 K) deformation using Ni Mishin Potential
# TEM2D Digital Sample

units       metal
boundary    p p p

atom_style  atomic
read_data       Ni_tem1.atoms
mass            1 58.69
#replicate 1 1 2
pair_style  eam/alloy
pair_coeff  * *  niyuri.pot   Ni

neighbor        2.0 bin
neigh_modify      delay 10

compute     new  all  temp

velocity    all  create 300.0 5812775 temp new
compute       centro  all centro/atom
compute       pea  all pe/atom
compute       stress  all stress/atom

dump            1 all custom  30000 dump.tensile id  x y z  c_centro c_pea
c_stress[2] c_stress[4]
#dump_modify     1 scale no
thermo           500
thermo_modify   lost warn  norm yes  temp new
fix              1 all npt 300.0 700.0 0.25 aniso  0.0 0.0  0.0 0.0  0.0 0.0
0.1 drag 0.1
fix              2 all temp/rescale 10 300.0 700.0 10.0 1.0
fix_modify  2 temp new
timestep    0.001
run         30000
unfix 1
unfix 2

fix              1 all npt 700.0 700.0 0.25 aniso  NULL NULL  0.0 0.0  0.0
0.0  0.1 drag 0.1
fix              2 all temp/rescale 10 700.0 700.0 10.0 1.0
fix              3 all deform 1000 x final -401.97 401.97  units box
fix_modify  2 temp new
timestep    0.001
run         450000
```

```
# Metal tensile test simulation (X-Tens Deformation up to 15% strain)
# Low temperature (300 K) deformation using Ni Mishin Potential
# TEM3D Digital Sample (with free surfaces)

units       metal
boundary    p p s

atom_style  atomic
read_data       Ni_thickfs.atoms
mass            1 58.69
#replicate 1 1 2
pair_style  eam/alloy
pair_coeff  * *  niyuri.pot   Ni

neighbor        2.0 bin
neigh_modify      delay 10

compute     new  all  temp

velocity    all  create 300.0 5812775 temp new
compute       centro  all centro/atom
compute       pea  all pe/atom
compute       stress  all stress/atom
compute       cn  all  coord/atom  3.0

dump            1 all custom  15000 dump.tensile id  x y z  c_centro c_pea
c_stress[2] c_stress[4] c_cn
#dump_modify     1 scale no
thermo           500
thermo_modify   lost warn  norm yes  temp new
#fix               1 all nve
fix              1 all npt 300.0 300.0 0.25 aniso  NULL NULL  0.0 0.0  NULL
NULL  0.1 drag 0.1
fix              2 all temp/rescale 10 300.0 300.0 10.0 1.0
fix              3 all deform 1000 x final -320.47 320.47  units box
fix_modify  2 temp new
timestep    0.001
run         450000
```

A2. Cracking summary table

Cracking results for all the computer-generated samples tested at 300K. All cracks observed were intergranular.

Sample	Tensile Direction	Crack No.	Angle (°)	Boundary Type	Boundary ID	Strain	Near Triple Junction?	Schmid Grain A	Schmid Grain B	Schmid Difference
9g40n	X	1	89.2	RHA	GB1-9	6%	Yes	0.47	0.37	0.10
	Y	1	81.7	RHA	GB1-5	8%	Yes	0.47	0.45	0.02
		2	65.1	RHA	GB4-7	8%	No	0.48	0.48	0.00
TEM1 (2D)	X	1	66.9	RHA	GB 6-8	5%	Yes	0.19	0.28	0.09
		2	70.5	RHA	GB 7-8	6%	Yes	0.20	0.28	0.08
	Y	1	63.9	RHA	GB 7-8	4%	No	0.20	0.28	0.08
		2	85.4	RHA	GB 1-5	5%	Yes	0.34	0.29	0.05
TEM2 (3D)	X	1	80.7	RHA	GB 2-5	8.0%	Yes	0.47	0.49	0.02
	Y	1	86.9	RHA	GB 1-5	7.0%	Yes	0.47	0.49	0.02